Radiative Signature of Absorbing Aerosol over the Eastern Mediterranean Basin

Amit Kumar Mishra[1], Klaus Klingmueller[2], Erick Fredj[1], Jos Lelieveld[3], Yinon Rudich[1,*], Ilan Koren[1,*]

[1]Department of Earth and Planetary Sciences, Weizmann Institute of Science, Rehovot 76100, Israel

[2] The Cyprus Institute, PO Box 27456, 1645 Nicosia, Cyprus

[3] Max Planck Institute for Chemistry, PO Box 3060, 55020 Mainz, Germany

*Correspondence: yinon.rudich@weizmann.ac.il, ilan.koren@weizmann.ac.il

Abstract

The effects of absorbing aerosols on the atmospheric radiation budget and dynamics over the eastern Mediterranean region are studied using satellites and ground-based observations, and radiative transfer model calculations, under summer conditions. Climatology of aerosol optical depth (AOD), single scattering albedo (SSA) and size parameters were analyzed using multi-year (1999-2012) observations from MODIS, MISR and AERONET. CALIOP-derived aerosol vertical distributions and their classifications are used to calculate the AOD of 4 dominant aerosol types: dust, polluted dust, polluted continental and marine aerosol over the region. The seasonal mean (June – August, 2010) AODs are 0.22 ± 0.02, 0.11 ± 0.04, 0.10 ± 0.04 and 0.06 ± 0.01 for polluted dust, polluted continental, dust and marine aerosol, respectively. Changes in the atmospheric temperature profile as a function of absorbing aerosol loading were derived for the same period using observations from the AIRS satellite. We inferred heating rates in the aerosol layer of $\sim1.7\pm0.8$ Kday^{-1} between 925 and 850 hPa, which is attributed to aerosol absorption of incoming solar radiation. Radiative transfer model (RTM) calculations show significant atmospheric warming for dominant absorbing aerosol over the region. A maximum atmospheric forcing of $+16.7\pm7.9$ Wm^{-2} is calculated in the case of polluted dust, followed by dust ($+9.4\pm4.9$ Wm^{-2}) and polluted continental ($+6.4\pm4.5$ Wm^{-2}). RTM-derived heating rate profiles for dominant absorbing aerosol show warming of $0.1 – 0.9$ Kday^{-1} in the aerosol layer (<3.0 km altitudes), which primarily depend on AODs of the different aerosol types. Diabatic heating due to absorbing aerosol stabilizes

40 the lower atmosphere, which could significantly reduce the atmospheric ventilation.

41 These conditions can enhance the 'pollution pool' over the eastern Mediterranean.

42 **Key words:** Absorbing Aerosol, Atmospheric Heating, Dust, Pollution, Mediterranean

43 basin, AIRS, MODIS, CALIPSO.

44

45 1 Introduction

46   Atmospheric aerosols constitute an important component of Earth's radiation

47 balance and in determining cloud properties and consequences (Forster et al., 2007). The

48 uncertainties related to the aerosol radiative forcing are large and have imposed a major

49 challenge in understanding the anthropogenic role in climate change (Forster et al., 2007;

50 Stevens and Feingold, 2009; Leibensperger et al., 2012). These large uncertainties are

51 mainly associated with great spatial and temporal variability of aerosol composition and

52 loading. Aerosols affect the radiation budget both directly through scattering and

53 absorption of solar radiation and indirectly through modifying cloud microphysics

54 (Kaufman et al., 2001; Kaufman and Koren, 2006; Khain, 2009; Li et al., 2011; Seiki and

55 Nakajima, 2013). By absorbing solar radiation, aerosol can modify atmospheric stability

56 and hence affect cloud formation and dissipation that could possibly impact precipitation

57 (Ramanathan et al., 2005; Koren et al., 2008). Recent studies (Davidi et al. 2009; Wang,

58 2010; Davidi et al., 2012) have shown that elevated biomass burning aerosol over the

59 Amazon and dust particles (Saharan Aerosol Layer) over the Atlantic Ocean can lead to a

60 temperature increase of that layer by 2-4 K. These results call for more studies on the

3

61   possible effects of absorbing aerosol over other climatically sensitive regions of the

62   world.

63   The Mediterranean basin is a crossroad of different aerosol types (Lelieveld et al.,

64   2002; Markowicz, et al., 2002), which makes it an ideal natural laboratory to study the

65   effect of different types of absorbing aerosol on the regional and local radiation budget

66   and the consequences for atmosphere dynamics in the region. In general, this region is

67   significantly impacted by variety of aerosol types including mineral dust from Africa and

68   Middle East, pollution from Europe and nearby coastal regions, and background marine

69   aerosol (Moulin et al., 1998; Lelieveld et al., 2002, Gerasopoulos et al., 2006; Erel et al.,

70   2006; Di Iorio et al., 2009). The seasonality of aerosol types over the basin (Vrekoussis et

71   al., 2005; Pace et al., 2006; Marey et al., 2011) calls for investigation of the contribution

72   of absorbing aerosols to total aerosol radiative forcing. Moreover, the absorption of

73   incoming solar radiation by aerosols is greatly enhanced during the summer cloud-free

74   conditions due to the intense solar radiation. Mallet et al (2013) recently reported the

75   dominance of absorbing aerosol over the eastern part as compared to the western part of

76   the basin during the summer season, indicating that the absorbing nature of the aerosol is

77   dominant during summer. Absorbing aerosols were shown to increase the absorption of

78   solar radiation in the atmospheric column $(+11.1 \text{Wm}^{-2})$ and reduce the surface radiation

79   (-16.5 Wm^{-2}) inducing significant atmospheric warming and surface cooling over the

80   region (Papadimas et al., 2012).

81   Markowicz et al. (2002) found that the daily averaged atmospheric warming (+11.3

82   Wm^{-2}) and surface cooling (-17.9 Wm^{-2}) by summertime absorbing aerosol over the

83   Mediterranean are similar to the highly absorbing south Asian haze observed over the

4

84   Arabian Sea. Significant negative radiative forcing at the surface has also been reported

85   in dust dominant (-70.8 Wm^{-2}) and pollution dominant (-39.1 Wm^{-2}) case studies (Meloni

86   et al., 2003). Di Sarra et al. (2008) estimated that the average daily forcing (at the

87   surface) at the summer solstice and equinox for desert dust is -30 and -24 Wm^{-2},

88   respectively. Numerous other studies have also emphasized the significant role of

89   absorbing aerosol over the Mediterranean region (Kazadzis et al., 2009; Santese et al.,

90   2010; Di Biagio et al., 2010). Nevertheless, the inferences of these studies (atmospheric

91   warming and surface cooling due to absorbing aerosol) are derived from the calculation

92   of direct radiative forcing of aerosol using radiative transfer models mainly focused over

93   the Mediterranean island of Lampedusa, Crete or other Southern European countries. To

94   the best of our knowledge there have been no direct measurement of absorbing aerosol's

95   effect on the atmospheric temperature profile (i.e. change in atmospheric stability due to

96   absorbing aerosol loading) over the region nor attribution of it to different aerosol types.

97   Given the importance of the strong atmospheric absorption in the eastern

98   Mediterranean Basin, we have conducted a comprehensive study in order to characterize

99   the effects of atmospheric absorption of the different aerosol types on the atmospheric

100 stability and the resulting climatic effects over the region. To that end, long term

101 climatology (~10 year) of aerosol optical (extinction/absorption) and microphysical

102 properties (size parameters) has been established for the Eastern Mediterranean. The

103 effect of absorbing aerosol on tropospheric atmospheric stability has been studied using

104 the state of the art remote sensing methodology (satellite measure of aerosol loading and

105 temperature profile). Finally, the observed properties of different aerosol types have been

106 used in a radiative transfer model to estimate the resulting climate effects.

107

2 Methodology

Combined analyses of multiple datasets, derived from satellite, ground based measurements and radiative transfer model results, are used in this study. We focused on the eastern Mediterranean between 24.5^0E to 34.5^0E and 32.5^0N to 35.5^0N. The rectangular box over the eastern Mediterranean basin in Fig. 1 represents the region of interest (ROI) for the present study. The analyzed ROI (area encompasses ~5000 km^2) has been chosen due to (1) focus on the eastern part of the basin which is significantly impacted by near and distant variable aerosol sources (Vrekoussis et al., 2005; Melin and Zibordi, 2005; Dermian et al., 2006; Basart et al., 2009) and (2) reliability of the satellite products over the marine regions (surface albedo effect). The flow chart of methodology is given in Fig. 2 which is explained as follows:

Monthly averaged (2002-2012) Moderate Resolution Imaging Spectroradiometer (MODIS; $1° \times 1°$) and Multi-angle Imaging SpectroRadiometer (MISR; $0.5° \times 0.5°$) level 3 derived aerosol properties (Diner et al. 1998; Kahn et al., 2005; Levy et al., 2007; Remer et al., 2008) have been used to study the long term climatology over ROI. We have also used $1° \times 1°$ gridded MODIS-derived daily averaged aerosol optical depth (AOD at 550 nm) and Fine Fraction (*ff*) along with the Atmospheric Infra-Red Sounder (AIRS)-derived temperature ($1° \times 1°$ spatial resolution) at 4 pressure levels: 1000, 925, 850 and 700 hP (Aumann et al., 2003; Diao et al., 2013) to analyze the absorption effect of aerosol on atmospheric stability. More details on accuracy and validation of AIRS temperature product can be found elsewhere (Davidi et al., 2009, and references therein).

129   The AIRS temperature data are sorted according to AOD and divided into equally spaced

130   bins of AOD. Both MODIS and AIRS fly on the Aqua platform (~01:30 p.m. LT),

131   whereas MISR is on board Terra platform (~10:30 a.m. LT).

132   24 Aerosol Robotic Network (AERONET) sites have been chosen to represent the

133   long term (1999-2012) climatology of aerosol absorption and the size properties of the

134   dominant aerosol types over the basin. We have used level 2 data of the single scattering

135   albedo (SSA), AOD and asymmetry parameter (ASYM) at 4 wavelengths (440, 675, 870

136   and 1020 nm). Following Russell et al. (2010), aerosol absorption optical depth (AAOD

137   = [1-SSA]*AOD) follows a relatively smooth decrease with wavelength (λ) and can be

138   approximated with power-law wavelength dependence (AAOD ~ λ^{-AAE}). By convention,

139   absorption Angstrom exponent (AAE) is the negative of the slope of the absorption on a

140   log-log plot. In the same manner, the extinction Angstrom exponent (EAE) is calculated

141   by power-law wavelength approximation (AOD~ λ^{-EAE}), which is used as a size

142   parameter of aerosol particles. The details of the AERONET products and associated

143   error analyses can be found elsewhere (Holben et al., 1998; Eck et al., 1999; Dubovik et

144   al., 2000; Sinyuk et al., 2012; Eck et al., 2013). The selection of AERONET sites was

145   based on extensive data volume (>2.5 year) and geographical locations among aerosol

146   source regions around the Mediterranean Basin (Fig. 1). Each site is classified (following

147   Mallet et al., 2013) as either dust affected or pollution dominated site based on the source

148   regions and known seasonal changes in aerosol types over these regions (Holben et al.,

149   2001; Tanre et al., 2001; Dubovik et al., 2002; Reid et al., 2003; Melin and Zibordi,

150   2005; Derimian et al., 2006; Eck et al., 2010; Giles et al., 2012; Mallet et al., 2013;

151   Marconi et al., 2014). Dust affected sites are depicted by red circles and pollution

dominated sites are shown by blue circles in Fig. 1. More details on site classification can be found in Mallet et al. (2013). Fig. 3 plots averaged level 2 AOD_{440} and $AAOD_{440}$ with $EAE_{440-870}$ for all 24 sites. Red triangle represents the dust affected sites whereas blue circles show pollution dominated sites. Relatively higher AAOD and lower EAE of dust affected sites (except Forth Crete and Erdemli; see Table S1) manifest the effect of dust particles in absorption and size parameters. We synthesize the optical models for the three different aerosol types (dust, polluted dust and polluted continental) over the Mediterranean. We have classified aerosol events based on daily AERONET observations. Our classification was done strictly based on the size parameter (EAE). For aerosol classification as dust, we used all dust-dominated sites data with EAE<0.6. Dust model for individual sites can be seen in Fig. S1a. For classification as polluted dust (mixed aerosol) we included Athens and Messina (possible mixing sites) with all other dust dominated sites and selected AERONET data with 0.7<EAE<1.1. Pollution (polluted continental) has been characterized as EAE >1.4 for all pollution dominated sites. Polluted continental model for individual sites can be seen in Fig. S1b. The optical models for all three different absorbing aerosol types are presented for summer season (see section 3.1). We treat DJF as winter, MAM as spring, JJA as summer, and SON as autumn in this study.

In addition, we used the particle extinction coefficient (σ_{ext} at 532 nm; L2_V3.01 product) profiles from the Cloud-Aerosol Lidar with Orthogonal Polarization (CALIOP) on-board the Cloud-Aerosol Lidar and Infrared Pathfinder Satellite Observations (CALIPSO), to estimate the vertical profiles of the different aerosol types (Winker et al., 2003; Young and Vaughan, 2009). The CALIOP aerosol identification algorithm (Omar

175   et al., 2009) also provides details about the vertical profile of the different aerosol types.

176   Total 73 CALIPSO overpasses (37-day and 36-night time) over the ROI have been

177   analysed in this study. Although day-time profiles have relatively higher noise than night-

178   time profiles, both profiles have been used to maximize the number of observation in our

179   study. To minimize possible artifacts due to cloud contamination in the extinction signals,

180   a standard scheme (Winker et al., 2013; Fig. S2) has been used to screen out all spurious

181   points in our datasets (about 5% data was rejected). CALIOP-generated extinction

182   profiles have been used in the calculation of AOD ($\tau = \int_{z_1}^{z_2} \sigma_{ext} \, dz$) for various types of

183   aerosol over the ROI.

184   We performed clear-sky solar irradiance, covers both short wavelength and long

185   wavelength (0.25 – 20 μm), computations using the Santa Barbara DISORT Atmospheric

186   Radiative Transfer (SBDART) code (Ricchiazzi et al., 1998), which uses the discrete

187   ordinates radiative transfer (DISORT) integration of the radiative transfer equations

188   (Stamnes et al., 1988). This code includes multiple scattering in a vertically

189   inhomogeneous, non-isothermal plane-parallel medium, and is computationally efficient

190   in resolving the radiative transfer equation (McComiskey et al. 2008). The SBDART

191   characterizes atmospheric aerosol radiative effects using as input the solar zenith angle

192   (0^0<sza<90^0 with 5^0 interval, and sza= 60^0 is used for averaged day-time calculation), the

193   spectral AOD, the spectral SSA, and the spectral ASYM.

194   To perform aerosol radiative forcing calculations in the 0.25 – 20 μm wavelength

195   range, aerosol properties in the entire wavelength region (0.25 – 20 μm) are necessary.

196   Since the measured AERONET aerosol optical properties are only available in the visible

9

197   and near-infrared wavelength range (~0.4 – 1.0 µm), we used AERONET observed

198   particle size distributions and refractive indices (0.4-1.0 µm) to estimate the aerosol

199   optical properties in the entire wavelength region (0.25 – 20 µm). To extrapolate the

200   refractive indices, we assume that the three aerosol types (dust, polluted dust and polluted

201   continental) are internal mixtures of components with known short-wave and long-wave

202   refractive indices. As mixing rule relating the refractive indices of mixture and

203   components, we used the volume averaged refractive index mixing rule. The components

204   assumed are: mineral dust and water for dust dominated aerosol; mineral dust, black

205   carbon and water for polluted dust; ammonium sulphate, black carbon and water for

206   polluted continental aerosol. In the latter case, ammonium sulphate is representative for

207   various components with similar refractive indices. The refractive indices of the

208   components are taken from Hess et al. (1998) for black carbon and mineral dust (SW),

209   Rothman et al. (2005) for ammonium sulphate and water and I. N. Sokolik (unpublished

210   data, 2005) for mineral dust (LW). The volume fractions are chosen such that the

211   refractive indices integrated over the wavelengths range of the observations (440 nm -

212   1020 nm) agree with the observed AERONET values. We obtain the following mean

213   volume fractions: 79.6 % mineral dust, 20.4 % water (dust); 38.5 % ammonium sulphate,

214   1.7 % black carbon, 59.8 % water (polluted continental); 60 % mineral dust, 0.5 % black

215   carbon, 39.5 % water (polluted dust). Using these volume fractions combined with the

216   refractive indices of the components and the observed particle size distributions, we

217   compute the aerosol optical properties. SCATTNLAY (Peña and Pal, 2009) Mie code is

218   employed for calculations of optical properties (AOD, AAOD, SSA, ASYM). To obtain

219   an error estimate, the standard deviation of the observations is propagated using jackknife

10

220 resampling (Wu, 1986). The output AODs for each aerosol types is scaled with CALIOP-

221 derived AOD.

222   The spectral SSA and the spectral ASYM are obtained from the abovementioned

223 procedure for different dominant aerosol types, whereas the vertical distributions of

224 aerosol types and AOD are supplied from CALIOP measurements. The atmospheric

225 model (McClatchey et al., 1972; Ricchiazzi et al., 1998) input was set as "Mid-Latitude

226 Summer Atmosphere". SBDART characterized 'ocean water' surface type was used to

227 parameterize the spectral albedo of surface (Tanré et al. 1990; Ricchiazzi et al., 1998).

228 The instantaneous values of aerosol radiative forcing (ΔF_{aer}) have been derived as $\Delta F_{aer} =$

229 $(F^{\downarrow} - F^{\uparrow}) - (F_0^{\downarrow} - F_0^{\uparrow})$, where F and F_0 denote the global irradiances with aerosol and

230 without aerosol, respectively. The arrows indicate the direction of the global irradiances

231 (down and up).

232

233 **3 Results and Discussion**

234 **3.1 Aerosol climatology**

235   Fig. 4 shows the 10 year (2002-12) monthly averaged variation of MODIS- and

236 MISR-derived aerosol optical depth and MODIS-derived cloud fraction (CF) over the

237 ROI. Both instruments show similar trend of aerosol loading with some discrepancies in

238 the averaged values. Possible explanations for these discrepancies in AOD are (1) the

239 instruments footpath cover different areas; (2) the overpass time of the 2 platforms is

240 different; and (3) technical reasons such as different retrieval algorithms (Kahn et al.,

241 2007), different processing methods (Abdou et al., 2005) and calibration. A detailed

242   discussion about aerosol measurement differences between these two sensors can be

243   found elsewhere (Kahn et al., 2007; Xiao et al., 2009; Shi et al., 2011). A significant

244   seasonal variability in aerosol loading with maximum in spring (April) and minimum in

245   winter (more exactly from November to January) is found over the ROI. The ten year

246   average seasonal mean AODs are 0.24-0.25, 0.20-0.23, 0.17-0.19 and 0.17-0.18 in spring,

247   summer, autumn and winter, respectively. This seasonal dependence is explained by the

248   seasonal variability in the major sources of aerosol loading over the Mediterranean that is

249   a function of synoptic meteorology (Lelieveld et al., 2002; Vrekoussis et al., 2005; Pace

250   et al., 2006; Kallos et al., 2007). Among all seasons, the summertime eastern

251   Mediterranean is characterized by a relatively minor cloud fraction (<0.15) and small

252   AOD variability at intra-seasonal scale (Fig. 4). Due to the cloud-free conditions, high

253   radiation intensity and less variability in aerosol loading during the summer, we have

254   chosen this season to study the climatic effects of absorbing aerosol over the ROI. The

255   another reason for choosing only summer season is that there are much less AERONET

256   level-2 absorption data during other seasons (Mallet et al., ACP, 2013). The seasonal

257   (summer) mean of AOD over the ROI for 10 years (2003-2012) are given in Table 1. The

258   summertime mean AODs vary between 0.19 and 0.25 in the span of 10 years. The

259   maximum and minimum AOD have been observed in 2010 and 2012, respectively. The

260   ten year averaged (2003-12) AOD is 0.21±0.02 in summer season over the ROI.

261   The summer-time AERONET-derived absorption and size properties for each site

262   are presented in Table 2. The average AAE values are in the range of 0.95-2.24 and 0.93-

263   1.58 for dust affected and pollution dominated sites respectively. Relatively higher values

264   of AAE (2.24) for Lampedusa as compared to other dust dominated sites could be

12

265 understood as the island is in close proximity to North Africa and could be more affected

266 by dust rather than pollution from Europe. However, the explanation of this high AAE

267 value of Lampedusa needs more deep introspection. Relatively lower values of AAE and

268 higher values of EAE of Erdemli, Sede Boker and Nes Ziona amidst other dust affected

269 sites can be understood as these sites are more affected by pollution than dust during

270 summer season (also manifested by larger SSA_{440} values). The size parameter (EAE)

271 shows lower values (0.82-1.39) for dust-affected sites and larger values (1.21-1.63) for

272 pollution dominant sites. These absorption and size properties are well within the range

273 of earlier reported values of worldwide dominant aerosol types (Dubovik et al., 2002;

274 Giles et al., 2012). The pollution dominated sites show slightly higher values of SSA_{440}

275 in the range of $0.91 - 0.95 \pm 0.04$ except Potenza. Recently, Mallet et al. (2013) have

276 shown that the Mediterranean urban-industrial aerosol appears moderately absorbing

277 ($SSA_{440} \sim 0.94 - 0.95 \pm 0.04$) in most cases except for Rome and Athens ($SSA_{440} \sim 0.89 -$

278 0.90 ± 0.04) where the aerosol appears to be more absorbing. The differences of optical

279 properties in this study and Mallet et al. (2013) can be understood as Table 2 depicts the

280 averaged properties for summer season only whereas Mallet et al. (2013) consider the

281 entire data set. However, Table S1 well corroborates with the findings of Mallet et al.

282 (2013). The role of dust in summer could be seen by comparing the summer means

283 (Table 2) and overall means (Table S1) of EAE for dust affected sites situated in western

284 basin (Blida, Malaga, Granada etc.). Dust events during summer are likely to decrease the

285 EAE values over these sites. However, the eastern basin sites are more influenced by

286 pollution as seen from increased values of EAE in summer as compared to overall means.

13

287   As we can see from the Table 2 that the optical properties of different sites in two

288   different categories shows great variability. We have characterized dust (EAE<0.6),

289   polluted dust (0.7<EAE<1.1) and polluted continental (EAE>1.4) aerosol using the size

290   parameter to separate these three classes as discussed in the methodology section. The

291   possible reason for this variability can be understood since the Mediterranean basin is a

292   cross-road of different aerosol types that mix in variable concentrations at different

293   locations. Fig. 5 presents the spectral variation of the summer-time averaged SSA,

294   AAOD, ASYM and volume size distribution of dominant absorbing aerosol types over

295   the Mediterranean Basin. All four properties show three different classes of aerosol

296   optical model with possible variance. The standard deviation in SSA at different

297   wavelengths shows relatively higher values for polluted dust and pollution aerosols.

298   However, the spectral shapes of SSA manifest the differences in absorption properties of

299   these three different aerosol classes which can be also seen in AAOD plot. The spectral

300   shape of the SSA for different aerosol types shows similar variation as reported in Russell

301   et al. (2010). As SSA is an intrinsic property of aerosol and does not depend on the

302   loading, it is used to separate the absorbing effect of dust, polluted dust and pollution in

303   radiative transfer scheme (section 3.4). The optical properties for all three aerosol types

304   in $0.25 - 20$ μm wavelength region (as discussed in methodology section) are given in

305   Fig. S3.

306

307   **3.2 Spatial and vertical distributions of aerosol during summer**

14

308   As summer 2010 shows all range of AOD (from low to high values), it has been

309   chosen for the analyses over the eastern Mediterranean basin. The seasonal mean of

310   MODIS-derived AOD is 0.25±0.12 over the ROI during summer 2010. Fig. 6 shows the

311   intra-seasonal variability of spatial distribution over the Mediterranean basin during

312   summer 2010. In terms of AOD spatial variability, all three months show significantly

313   different distribution of aerosol loading across the basin. In June, almost the entire basin

314   shows significantly higher aerosol loading (0.2-0.5) with a maximum in the south-west

315   part of the basin, whereas in July and August, the maximum aerosol loading is

316   concentrated in the eastern part of the basin. Over the Eastern basin, June and August are

317   associated with higher aerosol loading (AOD>0.2) as compared to July (AOD<0.2). The

318   MODIS-retrieved Fine Fraction (*ff*) provides a good idea about the size of particles

319   suspended in the atmosphere. Fig. 7 shows the relative frequency of occurrence of *ff* in all

320   three months of summer 2010.   The frequency of occurrence of higher values (>0.5) of *ff*

321   increases as the months progressed from June to August, indicating the increase in fine

322   mode particles as the summer progressed. This intra-seasonal spatial variability can be

323   explained as different air masses that come from Africa, Europe or the Middle East

324   significantly change the aerosol properties over the basin. In general, the central and

325   eastern Mediterranean basin is impacted by frequent dust events from Africa during June

326   that significantly decrease during the rest of the season (Lelieveld et al., 2002). Moulin et

327   al. (1998) have nicely presented the dust seasonality over the Mediterranean basin (West,

328   Central and Eastern). They have found higher dust-AOD in spring (0.14±0.05) than that

329   in summer (0.10±0.04) for eastern basin, whereas central and western basin shows higher

15

330   dust loading in summer (0.18±0.06 and 0.14±0.04, respectively) than that in spring

331   (0.15±0.06 and 0.10±0.04, respectively) over the period 1983-1994.

332   Fig. 8a shows the CALIOP-retrieved monthly average aerosol extinction

333   distribution for June, July and August during summer 2010. There is maximum extinction

334   near the surface (0.12-0.15 km^{-1}) in all three months that decreases significantly above

335   1 km altitudes. June and August show elevated (up to 2-5 km) aerosol supporting the

336   earlier observation from MODIS measurements (long-range transport of dust from the

337   African and the Arabian regions). CALIOP-derived AOD also corroborated the MODIS

338   observations i.e. significantly higher AOD in August (0.25±0.12) and June (0.19±0.09) as

339   compared to July (0.16±0.10). Recently Ma et al. (2013) reported that CALIPSO AOD is

340   significantly lower than that of MODIS AOD over the major dust source regions (Sahara,

341   Gobi etc.) of the world. However, the difference between these CALIOP- and MODIS-

342   derived AOD's is minimal (~0.05-0.07) over the Mediterranean basin during the summer

343   season, which is also reflected in the present study. Oo and Holz (2011) demonstrated

344   underestimation of AOD in oceanic regions in which CALIOP identifies clean marine,

345   but the fine mode fraction from the MODIS suggests a mixture of fine and coarse

346   aerosols. Several attempts have been made to compare the CALIOP aerosol classification

347   with AERONET and airborne High Spectral Resolution Lidar (HSRL-1) (Mielonen et al.,

348   2009; Burton et al., 2013). While mentioning the good agreement in 63-80% of the cases

349   between the most common aerosol types, these studies have warned against uncritical use

350   of CALIOP classification in scientific studies. Before using the CALIOP aerosol

351   classification in our study, we performed a cross check using MODIS *ff* over the ROI.

352 Fig. 9 shows the assessment of MODIS *ff* for three different scenarios of dominant

353 aerosol loading (dust, polluted dust and polluted continental) over the ROI. The mean

354 values of *ff* are 0.44±0.11, 0.55±0.12 and 0.64±0.17 for the dust, polluted dust and

355 polluted continental dominant aerosol classes, respectively. Earlier studies have reported

356 MODIS *ff* in the range of 0.25 – 0.45 for marine aerosols, 0.37 – 0.51 for dust, and 0.83 –

357 0.92 for anthropogenic aerosols over the various oceanic regions of the world (Kaufman

358 et al., 2005; Yu et al., 2009; Jones and Christopher, 2007; 2011). Relatively lower values

359 of *ff* are found in our cases (as compared to above-mentioned studies). These could be

360 understood as marine aerosols are present in all three cases in our study (Fig. 9, black

361 circles), which would likely decrease the average *ff* values for all three cases. Therefore,

362 distribution of *ff* as compared to other above-mentioned studies is in close agreement

363 with the aerosol classification for this present study.

364   The average vertical distributions of dominant aerosol types over the eastern

365 Mediterranean are presented in Fig. 8b (standard deviations are presented in Fig. S4).

366 Dust and polluted dust aerosol are frequently found at higher (3-6 km) altitudes whereas

367 polluted continental and marine aerosol are located within boundary layer (below 1.0-2.0

368 km altitudes). The maximal extinction has been shown by mixed aerosol (polluted dust~

369 0.05-0.25 km^{-1}) followed by pollution (polluted continental~ 0.02-0.15 km^{-1}) in the lower

370 troposphere (below 2.0 km altitude). The vertical distributions of different aerosol types

371 from this study are well corroborated with Nabat et al. (2013), which have nicely

372 presented a 4-dimensional climatology of aerosol properties over the Mediterranean

373 Basin. The seasonal mean (2010 summer) AOD of different dominant aerosol types are

374   0.22±0.02, 0.11±0.04, 0.10±0.04 and 0.06±0.01 for polluted dust, polluted continental,

375   dust and marine aerosol, respectively. The higher contribution from polluted dust (mixed

376   pollution + dust) reflects the real scenario over the Mediterranean, where the probability

377   of mixing of anthropogenic pollution and natural dust is found to reach a maximum

378   during the summer season.

379   **3.3 The effect of absorption on the atmospheric temperature profile**

380   Fig. 10 (a) shows the binned scatter plot of MODIS-AOD versus AIRS-

381   Temperature of four different pressure levels (1000, 925, 850 and 700 hPa) for the

382   summer 2010. The seasonal mean altitudes representing the different pressure levels are

383   approximated using atmospheric sounding data at Bet Dagan in the eastern

384   Mediterranean (http://weather.uwyo.edu/upperair/sounding.html, Station number:

385   40179). As the AOD increases from lowest bin (0.07) to the highest (0.58), there is an

386   increase of ~4 ^{0}C for 925 hPa (green) and 850 hPa (red) and no statistically significant

387   changes (with respect to standard deviation) at 1000 hPa (blue) and 700 hPa (cyan). The

388   increase in average temperature during high aerosol loading (AOD>0.5) at 925 and 850

389   hPa can be attributed to enhanced heating due to absorbing particles in that layer. The

390   CALIOP-derived aerosol vertical profiles (Fig. 8b) have also shown that the highest

391   contributions of dominant aerosol are below 2 km altitude. The temperature difference

392   between 850 hPa and 1000 hPa level is a good measure of stability in lower troposphere

393   (Davidi et al., 2009). The mean temperature difference of ~8 ^{0}C (solid black arrow in Fig.

394   10a) in clean conditions (AOD~ 0.08) between 1000 and 850 hPa is significantly lower

395   than the standard adiabatic lapse rate (~14 ^{0}C for 1400 m). This indicates the stable

18

atmosphere over the Eastern Mediterranean. This average temperature difference decreases by two fold (~4 ^{0}C, dotted black arrow in Fig. 10a) in the case of high aerosol loading (AOD~0.58), indicating that the diabatic heating in the presence of absorbing aerosol substantially increased the already existing stability of the lower troposphere. However, this role of absorbing aerosol is counteracted in the upper levels (between 850 - 700 hPa), where it adds instability to the already stable atmosphere (solid and dotted pink arrow in Fig. 10a). Fig. 10a shows that the difference between the temperatures at 850 hPa and 925 hPa is independent of aerosol loading, i.e. it is almost constant in the entire range of AOD (0.07 to 0.58). This observation suggests that the contribution of absorption from these two aerosol layers (at 850 hPa and 925 hPa) is almost similar in magnitude. Fig. S5 strengthened our abovementioned conclusion that the maximum observation due to absorbing aerosols (dust, polluted dust and polluted continental) occurs between ~400 and ~2200 m altitude range with almost similar relative frequency of occurrence. A similar effect of absorbing aerosol has been reported by Davidi et al., (2009; 2012), where they have found an increase of ~4 ^{0}C at 850 hPa in the case of smoke loading over the Amazon and ~5-6 ^{0}C increase in case of dust loading over the Atlantic. Ramanathan et al. (2001) has reported seasonal (JFM, 1999) and vertical averaged (0-3 km altitude) heating rate of ~0.3-0.6 K/day due to anthropogenic carbonaceous aerosols over the north Indian Ocean region. Mineral dust layers have also shown heating rate of about 0.5 K/day over the Arabian Sea and the Sahara coasts (Zhu et al., 2007).

417   While this correlation between AIRS temperature and MODIS AOD is substantial

418   with theoretical background related to diabatic heating of absorbing aerosol, one can

419   question the (1) AIRS artifact in temperature retrieval in case of dust (Maddy et al., 2012)

420   and (2) meteorology-driven changes in temperature, especially in the case of dust

421   outbreaks. Because of their large sizes (up to several micrometer), dust particles are able

422   to strongly interact with IR radiation and thus can affect the temperature retrieval in the

423   thermal spectrum (Pierangelo et al., 2004; DeSouza-Machado et al., 2006). In addition,

424   dust outbreaks are associated with dry and warm air, so it could carry the 'memory of

425   warm air' and could affect the temperature profiles during transport. We present the

426   relative frequency distribution of AOD occurrence (upper panel) and *ff* (lower panel) for

427   all observed data in Fig. 10b. The maximal relative frequency of AOD and *ff* appears

428   around 0.2 and 0.5-0.8, respectively. The mean values of temperature for each bin (Fig.

429   10a) integrate the effect of both fine and coarse particles. To address these issues, we

430   show similar analyses (same as Fig. 10a) for two different cases of MODIS *ff* (*ff* < 0.5

431   and *ff* > 0.5) in Fig. 11a. The number of sampled AOD pixels are comparably lower

432   (around half) in case of *ff*<0.5 than that of *ff*>0.5 (Fig. 11b). The *ff*<0.5 case associated

433   with dust (left panel) shows a slightly cooler atmosphere (explanations are given below)

434   than *ff*>0.5 case (right panel) all along the profile, but the trend of d(T)/d(AOD) is quite

435   similar in both cases (fine and coarse) and also represents the essence of Fig. 10a. From

436   this analysis, it is clear that the observed perturbation in temperature is apparent in both

437   coarse (dust) and fine absorbing particles (pollution). These observations further

438   strengthen the conclusion that the temperature increase is solely attributed to diabatic

439   heating by absorbing particles.

440   The plausible reason of cooler atmosphere in case *ff*<0.5 could be explained by Fig.

441   S6 (supplementary material). Fig. S6a shows that the AOD occurrence associated with

442   large particles is maximal in June as compared to other two later months or in other

443   words June month is highly impacted by dust events as compared to rest of season. Also

444   the mean temperature climatology shows a gradual increase as days progressed from June

445   to August. The daily mean values of AOD did not show any definite pattern with

446   temperature except few events in June and August (marked as double headed arrow). All

447   above mentioned analysis suggest that the coarse particles (dust events) dominant in early

448   summer season which is also characterized by slightly lower atmospheric temperature.

449   This could be a plausible reason of slightly lower atmospheric temperature in case of

450   coarse particles (*ff*<0.5) than that in fine particle case (*ff*>0.5) in Fig. 11a.

451

452   **3.4 Atmospheric heating due to different aerosol types: model assessment**

453   The strong dependence of aerosol direct radiative forcing (ADRF) at top of the

454   atmosphere (TOA) and at the surface (SRF) on solar zenith angle (sza) has well observed

455   by Boucher et al. (1998). In this study, the variation of radiative forcing of aerosol types

456   (dust, polluted dust and polluted continental) with solar zenith angle (SZA) at TOA, at

457   SRF and in the atmosphere (ATM) are given in Fig. S7 (supplementary material). Our

458   results agree with those of Boucher et al. (1998). In spite of the strong variability of

459   ADRF (at TOA and SRF) with sza, we used sza=60^0 to show our results for daytime

460   average (an approximation) because we compare our model assessment with the AIRS vs

461   MODIS analyses, which use instantaneous observations at 1.30 PM (LT) for each day. It

462   is worth mentioning that using a single sza= 60^0 (that is close to the maximum

463   instantaneous DRE) overestimates the calculated DRE as compared to cosine of sza

464   weighted mean DRE at TOA and at SRF, but in the atmosphere (ATM) it will be slightly

465   underestimated (Fig. S8).

466   Fig. 12 shows the clear-sky daytime averaged (sza=60^0) aerosol radiative forcing

467   (ΔF_{aer}) of dominant aerosol types (dust, polluted dust, polluted continental and marine) at

468   the surface (SRF), at the top of the atmosphere (TOA) and in the atmosphere (ATM)

469   during summer 2010 over the Eastern Mediterranean. The atmospheric forcing of aerosol

470   is the difference between forcing at TOA and SRF [$(\Delta F_{aer})_{ATM} = (\Delta F_{aer})_{TOA} - (\Delta F_{aer})_{SRF}$].

471   The error bars show the total uncertainties in radiative forcing due to the uncertainty in

472   the input parameters. We examined the dependence of forcing on each property, AOD,

473   SSA and g (sensitivity analyses of forcing to various parameters) separately (Fig. S9).

474   The sensitivity analyses have shown that the aerosol forcing values strongly depends on

475   the AOD values as compared to any other properties (SSA and g). The total uncertainty

476   in forcing, owing to the combined influence of the uncertainties in the various properties

477   is determined under the assumption that these uncertainties are not correlated

478   (McComiskey et al., 2008).

479   All dominant aerosol types show negative radiative forcing at both the surface and

480   the TOA. The higher values of $|(\Delta F_{aer})_{SRF}|$ than that of $|(\Delta F_{aer})_{TOA}|$ are a result of the

481   positive atmospheric forcing for almost all aerosol types, which reflect the absorbing

482   behavior of these aerosols. However, this value ($(\Delta F_{aer})_{ATM}$) is close to zero in the case

483   of marine aerosol. The forcing values at TOA and at the surface are largest for polluted

484   dust due to the high value of AOD. The maximal atmospheric forcing is observed in the

22

485   case of polluted dust (16.7±7.9Wm^{-2}) followed by dust (9.4±4.9 Wm^{-2}) and polluted

486   continental (6.4±4.5 Wm^{-2}) aerosol. The atmospheric radiative forcing efficiencies

487   (defined by radiative forcing for unit optical depth) are found to be slightly more in case

488   of dust (+86.2 Wm^{-2}) than polluted dust (+77.2 Wm^{-2}) and polluted continental (+62.5

489   Wm^{-2}). The significant positive radiative forcing for dominant absorbing aerosol

490   corroborated our earlier observations of heating in the atmosphere (section 3.3). Di

491   Biagio et al. (2010) showed that these atmospheric forcing (at the summer solstice) could

492   be increased up to +35 Wm^{-2} for desert dust (DD), +23Wm^{-2} for pollution (UI-BB) and

493   +34 Wm^{-2} for mixed aerosol (MA) in the highest aerosol loading for these classes (AOD~

494   0.88 for DD, 0.44 for UI-BB, and 0.45 for MA) over the Mediterranean region. The

495   regional mean values of aerosol forcing over the broader Mediterranean basin under clear

496   sky conditions have been found to be +7.4±3.3, +19.2±2.9, +20.1±1.1 and +7.7±4.0

497   Wm^{-2} for winter, spring, summer and autumn, respectively (Papadimas et al., 2012). The

498   global mean atmospheric forcing (SW) of dust has been recently reported to be in the

499   range of +1.57 to +1.73 Wm^{-2} using GEOS-Chem global three dimensional Chemical

500   Transport Model coupled with Fu-Lion-Gu (FLG) radiative transfer model (Zhang et al.,

501   2013). They also reported the FLG-derived radiative forcing over major dust prone

502   regions of world: Sahara (+15.22 Wm^{-2}), Gobi (+15.79 Wm^{-2}), Arabian Sea (+5.07

503   Wm^{-2}) and Eastern Asia (+4.96 Wm^{-2}).

504   Table 3 presents the daytime average aerosol radiative forcing in short wavelength

505   (SW: 0.25-4.0 μm) and long wavelength (LW: 4.0-20 μm) regime for dominant aerosol

506   types. The LW radiative forcing is positive both at SRF and TOA since aerosol produced

507   planetary and surface warming through interaction with infrared (IR) radiation. Fig. S10

508 shows radiative forcing of different aerosols types as a function of wavelength for both

509 SW and LW region. The importance of the particle size in the LW regime can be seen

510 from the Fig. S10 and Table 3, where dust and polluted dust (diameter up to several

511 micrometers) show higher forcing values as compared to polluted continental aerosol

512 (diameter less than 1 μm). It is worth noting that we cannot expect significant radiative

513 forcing of anthropogenic pollution in the LW region due to the small sizes of these

514 particles. Bergamo et al. (2008) have reported that the IR surface direct radiative forcing

515 of anthropogenic aerosol reach peak values close to 0.35 Wm^{-2} (significantly larger than

516 the TOA values) at most of the Mediterranean sites during summer and offset 3-6% of

517 the negative solar (SW) radiative forcing. Our results suggest that the role of absorbing

518 aerosol are mainly associated with the SW region, where it absorbs and scatters the

519 incoming SW solar radiation and thus produces the planetary and surface cooling effect.

520 However, LW radiative forcing at SRF offset about 11.3% and 8.6% of the negative solar

521 (SW) radiative forcing in case of dust and polluted dust, respectively.

522   Our results along with other earlier studies show significant atmospheric heating

523 due to different absorbing aerosol types over the Mediterranean basin. Moreover the

524 coupling of natural and anthropogenic pollution leads to higher heating in the

525 atmosphere. It is interesting to investigate how much atmospheric heating (in terms of

526 temperature change) and at which altitudes is contributed by absorbing aerosol. Fig. 13

527 shows the atmospheric heating rate (K/day) profiles of dust, polluted dust and polluted

528 continental over the eastern Mediterranean during summer 2010. Polluted dust shows the

529 maximal heating rate (0.2 – 0.9 K/day) in the lower troposphere (<2.0 km altitudes)

24

530 followed by the polluted continental (0.1 – 0.5 K/day) aerosol. We also found a relatively

531 small heating (<0.1 K/day) at high altitudes (>3.0 km), in the case of both dust and

532 polluted dust. The similarities in the shape of the vertical heating profiles (Fig. 13) and

533 aerosol extinction profiles (Fig. 8b) suggest that the aerosol optical depth distribution

534 plays a major role in the radiative forcing. Zhang et al. (2013) found that dust particles

535 could heat the atmosphere by more than 0.5 K/day over African and Asian source

536 regions. Huang et al. (2009) have also shown that atmospheric heating of dust particles

537 could reach up to 3 K/day in heavy dust layers over the Taklimakan Desert in

538 Northwestern China.

539

540 **4 Implications on regional atmospheric dynamics**

541 By a good approximation, we can consider that the absorbing properties of aerosol

542 are somewhat similar in all summer seasons and AOD is the main factor that affects the

543 aerosol diabatic heating (on yearly basis) over the ROI. Retrieval of the effect of

544 absorbing aerosol loading on atmospheric temperature profile reveals an increase of ~4

545 ^{0}C due to aerosol during hazy (AOD~0.58) conditions as compared to clean conditions.

546 The average diabatic heating due to absorbing aerosol over the ROI was ~1.7±0.8 K/day

547 in summer 2010. The diabatic heating of absorbing aerosol is presented in Table 4 for ten

548 years (2003-2012). SBDART calculations show significant diabatic heating (0.1-0.9

549 K/day) due to different absorbing aerosol in the lower troposphere. The overestimated

550 heating rate from AIRS vs MODIS observation as compared to model calculations is

551 attributed to the treatment of different aerosol types by the RTM, whereas the remote

552 sensing calculation combined the effect of all aerosol types present. In addition, the

553 different AOD used in both methods (CALIOP-derived in RTM and MODIS-derived in

554 other one) could be an important reason for these differences. By now, it is evident that

555 the absorbing aerosol is heating the atmospheric layers, so how is it going to affect or

556 modulate the summertime regional dynamics over the Eastern Mediterranean?

557   In general, the increase in temperature due to aerosol absorption stabilizes the lower

558 atmosphere, leading to the weakening of convection in the lower atmosphere and may

559 inhibit cloud formation (Ackerman et al., 2000). However, the summertime

560 Mediterranean atmospheric condition is already too stable to form convective clouds over

561 the region. The diabatic heating adds even more stability, which will significantly inhibit

562 the atmospheric ventilation and could protect the aerosol from meteorological dilution. In

563 other words, the absorbing aerosol loading over the significantly large area of the Eastern

564 Mediterranean Sea may create a low pressure in the lower atmosphere and may receive

565 more pollution from nearby high pressure regions. Hence, the effect of absorption

566 properties of the regional aerosols enhances the formation of a 'pollution pool' over the

567 region. Our results also suggest that the coupling between natural dust emissions and

568 pollution leads to stronger heating. This suggests that a policy to reduce anthropogenic

569 light absorbing pollution will have beneficial climatic impacts in the region. In a follow-

570 up study, we will investigate the climate effects of these absorbing aerosols in more detail

571 using the chemistry-climate coupled EMAC model.

572

573 **5 Conclusions**

574   A comprehensive study on the effects of absorbing aerosols on the regional

575   atmospheric dynamics over the eastern Mediterranean basin (between 24.5^0E to 34.5^0E

576   and 32.5^0N to 35.5^0N) has been carried out using the state-of-art remote sensing analyses

577   from multi-satellite and ground-based observations, coupled with a radiative transfer

578   model. The results of this study can be summarized as follows:

579   1. The seasonal mean MODIS-AODs (2010-2012) are in the range of 0.24-0.25, 0.20-

580   0.23, 0.17-0.19 and 0.17-0.18 in spring, summer, autumn, and winter, respectively.

581   2. The CALIOP-derived AODs of dominant aerosol types are 0.22 ± 0.02, 0.11 ± 0.04,

582   0.10 ± 0.04 and 0.06 ± 0.01 for polluted dust, polluted continental, dust and marine aerosol,

583   respectively.

584   3. Direct measurement of the effect of aerosol loading (MODIS) on atmospheric

585   temperature profiles (AIRS) shows a warming of $\sim1.7\pm0.8$ K/day in the aerosol layer,

586   which is likely due to direct absorption of incoming shortwave solar radiation.

587   4. RTM-derived results show maximal atmospheric heating for polluted dust (0.1-0.9

588   K/day) followed by polluted continental (0.1-0.5 K/day) in lower troposphere (<3.0 km).

589   5. In summer 2010, the daytime average atmospheric forcing is found to be $+16.7\pm7.9$,

590    $+9.4\pm4.9$ and $+6.4\pm4.5$ Wm^{-2} for polluted dust, dust and polluted continental aerosols,

591   respectively.

592   The findings from this study lead to a well approximated assessment of the effects

593   of absorbing aerosols, and the coupling of pollution and natural dust on the radiation

27

594   budget in the eastern Mediterranean. These results enable to formulate mitigation and

595   adaptation scenarios based on reliable observations and scientific understanding.

596

597   **Acknowledgements**

602   **References**

603   Abdou, W. A., Diner, D. J., Martonchik, J. V., Bruegge, C. J., Kahn, R. A., Gaitley, B. J.,

604   Crean, K.A., Remer, L.A., Holben, B.: Comparison of coincident Multiangle Imaging

605   Spectroradiometer and Moderate Resolution Imaging Spectroradiometer aerosol

606   optical depths over land and ocean scenes containing Aerosol Robotic Network sites.

607   J. Geophys. Res. Atmos., 110, D10S07, doi:10.1029/2004JD004693, 2005.

608   Ackerman, A. S., Toon, O. B., Stevens, D. E., Heymsfield, A. J., Ramanathan, V., and

609   Welton, E. J.: Reduction of tropical cloudiness by soot. *Science*, *288*(5468), 1042-

610   1047, 2000.

611   Aumann, H. H., Chahine, M. T., Gautier, C., Goldberg, M. D., Kalnay, E., McMillin, L.

612   M., Revercomb, H., Rosenkranz, P. W., Smith, W. L., Staelin, D. H., Strow, L. L.,

613   and Susskind, J.: AIRS/AMSU/HSB on the Aqua mission: Design, science objectives,

614   data products, and processing systems, IEEE T. Geosci. Remote., 41(2), 253–264,

615   2003.

616   Basart, S., Pérez, C., Cuevas, E., Baldasano, J. M., and Gobbi, G. P.: Aerosol

617   characterization in Northern Africa, Northeastern Atlantic, Mediterranean Basin and

618   Middle East from direct-sun AERONET observations, Atmos. Chem. Phys., 9, 8265-

619   8282, doi:10.5194/acp-9-8265-2009, 2009.

620   Bergamo, A., Tafuro, A. M., Kinne, S., De Tomasi, F., and Perrone, M. R.: Monthly-
621   averaged anthropogenic aerosol direct radiative forcing over the Mediterranean based
622   on AERONET aerosol properties, Atmos. Chem. Phys., 8, 6995-7014,
623   doi:10.5194/acp-8-6995-2008, 2008.

624   Boucher, O., Schwartz, S. O., Ackerman, T. P., Anderson, T. L., Bergstrom, B., Bonnel,
625   B et al.: Intercomparison of models representing direct shortwave radiative forcing by
626   sulfate aerosols. *Journal of Geophysical Research: Atmospheres (1984–*
627   *2012)*, *103*(D14), 16979-16998, 1998.

628   Burton, S. P., Ferrare, R. A., Vaughan, M. A., Omar, A. H., Rogers, R. R.,
629   Hostetler, C. A., and Hair, J. W.: Aerosol classification from airborne HSRL and
630   comparisons with the CALIPSO vertical feature mask, Atmos. Meas. Tech., 6, 1397-
631   1412, doi:10.5194/amt-6-1397-2013, 2013.

632   Davidi, A., A. B. Kostinski, I. Koren, and Y. Lehahn: Observational bounds on
633   atmospheric heating by aerosol absorption: Radiative signature of transatlantic dust,
634   Geophys. Res. Lett., 39, L04803, doi:10.1029/2011GL050358, 2012.

635   Davidi, A., Koren, I., and Remer, L.: Direct measurements of the effect of biomass
636   burning over the Amazon on the atmospheric temperature profile, Atmos. Chem.
637   Phys., 9, 8211-8221, doi:10.5194/acp-9-8211-2009, 2009.

638   Derimian, Y., A. Karnieli, Y. J. Kaufman, M. O. Andreae, T. W. Andreae, O. Dubovik,
639   W. Maenhaut, I. Koren, and B. N. Holben: Dust and pollution aerosols over the
640   Negev desert, Israel: Properties, transport, and radiative effect, J. Geophys. Res.
641   Atmos., 111, D05205, doi:10.1029/ 2005JD006549, 2006.

642   DeSouza-Machado, S. G., L. L. Strow, S. E. Hannon, and H. E. Motteler: Infrared dust
643   spectral signatures from AIRS, Geophys. Res. Lett., 33, L03801,
644   doi:10.1029/2005GL024364, 2006.

645   Di Biagio, C., di Sarra, A., and Meloni, D.: Large atmospheric shortwave radiative
646   forcing by Mediterranean aerosols derived from simultaneous ground-based and
647   spaceborne observations and dependence on the aerosol type and single scattering
648   albedo, J. Geophys. Res. Atmos., 115, D10209, doi:10.1029/2009JD012697, 2010.

649 Di Iorio, T., A. di Sarra, D. M. Sferlazzo, M. Cacciani, D. Meloni, F. Monteleone, D.
650   Fuà, and G. Fiocco: Seasonal evolution of the tropospheric aerosol vertical profile in
651   the central Mediterranean and role of desert dust, J. Geophys. Res. Atmos., 114,
652   D02201, doi:10.1029/2008JD010593, 2009.

653 Di Sarra, A., Pace, G., Meloni, D., De Silvestri, L., Piacentino, S., and Monteleone, F.:
654   Surface shortwave radiative forcing of different aerosol types in the Mediterranean,
655   Geophys. Res. Lett., 35, L02714, doi:10.1029/2007GL032395, 2008.

656 Diao, M., L. Jumbam, J., Sheffield, E. F. Wood, and Zondlo, M. A.: Validation of
657   AIRS/AMSU-A water vapor and temperature data with in situ aircraft observations
658   from the surface to UT/LS from 87^0N–67^0S, J. Geophys. Res. Atmos., 118, 6816-
659   6836, doi:10.1002/jgrd.50483, 2013.

660 Diner, D. J., J. C. Beckert, T. H. Reilly, C. J. Bruegge, J. E. Conel, R. A. Kahn, J. V.
661   Martonchik, T. P. Ackerman, R. Davies, S. A. W. Gerstl, H. R. Gordon, J.-P. Muller,
662   R. Myneni, P. J. Sellers, B. Pinty and M. M. Verstraete: Multiangle Imaging
663   Spectroradiometer (MISR) Instrument Description and Experiment Overview, IEEE
664   T. Geosci. Remote., 36(4), 1072-1087, doi:10.1109/36.700992, 1998.

665 Dubovik, O., A. Smirnov, B. N. Holben, M. D. King, Y.J. Kaufman, T. F. Eck, and
666   Slutsker, I.: Accuracy assessments of aerosol optical properties retrieved from
667   AERONET sun and sky-radiance measurements, J. Geophys. Res. Atmos., 105,
668   9791-9806, 2000.

669 Dubovik, O., B. N. Holben, T. F. Eck, A. Smirnov, Y. J. Kaufman, M. D. King, D. Tanre,
670   and I. Slutsker: Variability of absorption and optical properties of key aerosol types
671   observed in worldwide locations, J. Atmos. Sci., 59, 590–608, 2002.

672 Eck, T. F., B. N. Holben, J. S. Reid, O. Dubovik, A. Smirnov, N. T. O'Neill, I. Slutsker,
673   and S. Kinne: Wavelength dependence of the optical depth of biomass burning,
674   urban, and desert dust aerosols, J. Geophys. Res. Atmos., 104(D24), 31,333–31,349,
675   doi:10.1029/1999JD900923, 1999.

676 Eck, T. F., Holben, B.N., Reid, J. S., Mukelabai, M. M., Piketh, S. J., Torres, O., Jethva,
677   H. T., Hyer, E. J., Ward, D. E., Dubovik, O., Sinyuk, A., Schafer, J. S., Giles, D. M.,
678   Sorokin, M., Smirnov, A., and Slutsker, I.: A seasonal trend of single scattering

679   albedo in southern African biomass-burning particles: Implications for satellite
680   products and estimates of emissions for the world's largest biomass-burning source, J.
681   Geophys. Res. Atmos., 118, 6414-6432, doi:10.1002/jgrd.50500, 2013.

682 Eck, T. F., Holben, B.N., Sinyuk, A., Pinker, R. T., Goloub, P., Chen, H., Chatenet, B.,
683   Li, Z., Singh, R. P., Tripathi, S. N., Reid, J. S., Giles, D. M., Dubovik, O., O'Neill, N.
684   T., Smirnov, A., Wang, P., and Xia, X.: Climatological aspects of the optical
685   properties of fine/coarse mode aerosol mixtures, J. Geophys. Res. Atmos., 115,
686   D19205, doi:10.1029/2010JD014002, 2010.

687 Erel,Y., U. Dayan, R. Rabi, Y. Rudich, and M. Stein: Tracing Trans-Boundary Transport
688   of Pollutants by Mineral Dust, Environ. Sci. Technol., 40(9), 2996-3005, 2006.

689 Forster, P., V. Ramaswamy, P. Artaxo, T. Berntsen, R. Betts, D.W. Fahey, J. Haywood,
690   J. Lean, D.C. Lowe, G. Myhre, J. Nganga, R. Prinn, G. Raga, M. Schulz and R. Van
691   Dorland: Changes in Atmospheric Constituents and in Radiative Forcing. In: Climate
692   Change 2007: The Physical Science Basis, Contribution of Working Group I to the
693   Fourth Assessment Report of the Intergovernmental Panel on Climate Change
694   [Solomon, S., D. Qin, M. Manning, Z. Chen, M. Marquis, K.B. Averyt, M.Tignor and
695   H.L. Miller (eds.)], Cambridge University Press, Cambridge, United Kingdom and
696   New York, NY, USA, 2007.

697 Gerasopoulos, E., G. Kouvarakis, P. Babasakalis, M. Vrekoussis, J.-P. Putaud, and N.
698   Mihalopoulos: Origin and variability of particulate matter (PM10) mass
699   concentrations over the eastern Mediterranean, Atmos. Environ., 40, 4679–4690,
700   doi:10.1016/j.atmosenv.2006.04.020, 2006.

701 Giles, D. M., B. N. Holben, T. F. Eck, A. Sinyuk, A. Smirnov, I. Slutsker, R. R.
702   Dickerson, A. M. Thompson, and J. S. Schafer: An analysis of AERONET aerosol
703   absorption properties and classifications representative of aerosol source regions, J.
704   Geophys. Res. Atmos., 117, D17203, doi:10.1029/2012JD018127, 2012.

705 Hess, M., Koepke, P., and Schult, I.: Optical Properties of Aerosols and Clouds: The
706   Software Package OPAC, *Bulletin of the American Meteorological Society*, 79, 831-
707   44, 1998.

708 Holben, B. N., T.F. Eck, I. Slutsker, D. Tanre, Buis, J. P., Setzer, A., Vermote, E.,
709   Reagan, J. A., Kaufman, Y. J., Nakajima, T., Lavenu, F., Jankowiak, I., and Smirnov,
710   A.: AERONET–A federated instrument network and data archive for aerosol
711   characterization, Remote Sens. Environ., 66, 1–16, doi:10.1016/S0034-
712   4257(98)00031-5, 1998.
713 Holben, B. N., Tanre, D., Smirnov, A., Eck, T. F., Slutsker, I., Abuhassan, N. Newcomb,
714   W. W., Schafer, J. S., Chatenet, B., Lavenu, F., Kaufman, Y. J., Castle J. V., Setzer,
715   A., Markham, B., Clark, D., Frouin, R., Halthore, R., Karneli, A., O'Neill, N. T.,
716   Pietras, C., Pinker, R. T., Voss, K., and Zibordi, G.: An emerging ground-based
717   aerosol climatology: Aerosol optical depth from AERONET, J. Geophys. Res.
718   Atmos., 106(D11), 12067–12097, doi:10.1029/2001JD900014, 2001.
719 Huang, J., Fu, Q., Su, J., Tang, Q., Minnis, P., Hu, Y., Yi, Y., and Zhao, Q.: Taklimakan
720   dust aerosol radiative heating derived from CALIPSO observations using the Fu-Liou
721   radiation model with CERES constraints, Atmos. Chem. Phys., 9, 4011-4021,
722   doi:10.5194/acp-9-4011-2009, 2009.
723 Jones, T. A. and Christopher, S. A.: MODIS derived fine mode fraction characteristics of
724   marine, dust, and anthropogenic aerosols over the ocean, constrained by GOCART,
725   MOPITT, and TOMS, J. Geophys. Res. Atmos., 112, D22204,
726   doi:10.1029/2007JD00897, 2007.
727 Jones, T. A. and Christopher, S. A.: A reanalysis of MODIS fine mode fraction over
728   ocean using OMI and daily GOCART simulations, Atmos. Chem. Phys., 11, 5805-
729   5817, doi:10.5194/acp-11-5805-2011, 2011.
730 Kahn, R. A., Garay, M. J., Nelson, D. L., Yau, K. K., Bull, M. A., Gaitley, B. J.,
731   Martonchik, J. V., and Levy, R. C.: Satellite-derived aerosol optical depth over dark
732   water from MISR and MODIS: Comparisons with AERONET and implications for
733   climatological studies. J. Geophys. Res. Atmos., 112, D18205,
734   doi:10.1029/2006JD008175, 2007.
735 Kahn, R., Gaitley, B., Martonchik, J., Diner, D., Crean, K., and Holben, B.: MISR global
736   aerosol optical depth validation based on two years of coincident AERONET

observations. J. Geophys. Res. Atmos., 110, D10S04. doi:10.1029/2004JD00406, 2005.

Kallos, G., Astitha, M., Katsafados, P., and Spyrou, C.: Long-range transport of anthropogenically and naturally produced particulate matter in the Mediterranean and North Atlantic: Current state of knowledge, J. Appl. Meteorol. Climatol., 46, 1230–1251, doi:10.1175/JAM2530.1, 2007.

Kaufman, Y. J. and Koren, I.: Smoke and pollution aerosol effect on cloud cover, Science, 313, 355–658, 2006.

Kaufman, Y. J., Boucher, O., Tanre', D., Chin, M., Remer, L. A., and Takemura, T.: Aerosol anthropogenic component estimated from satellite data, Geophys. Res. Lett., 32, L17804, doi:10.1029/2005GL023125, 2005.

Kaufman, Y. J., D. Tanré, O. Dubovik, A. Karnieli, and L. A. Remer: Absorption of sunlight by dust as inferred from satellite and ground-based remote sensing, Geophys. Res. Lett., 28(8), 1479-1482, 2001.

Kazadzis, S., Kouremeti, N., Bais, A., Kazantzidis, A., and Meleti, C.: Aerosol forcing efficiency in the UVA region from spectral solar irradiance measurements at an urban environment, Ann. Geophys., 27, 2515–2522, doi:10.5194/angeo-27-2515- 2009, 2009.

Khain, A. P.: Notes on state-of-the-art investigations of aerosol effects on precipitation: a critical review, Environ. Res. Lett., 4(1), 015004, doi:10.1088/1748-9326/4/1/015004, 2009.

Koren, I., Martins, J.V., Remer, L.A., Afargan H.: Smoke Invigoration Versus Inhibition of Clouds over the Amazon, Science, 321(5891), 946-949, doi:10.1126/science.1159185 2008, 2008.

Leibensperger, E. M., Mickley, L. J., Jacob, D. J., Chen, W.-T., Seinfeld, J. H., Nenes, A., Adams, P. J., Streets, D. G., Kumar, N., and Rind, D.: Climatic effects of 1950–2050 changes in US anthropogenic aerosols – Part 1: Aerosol trends and radiative forcing, Atmos. Chem. Phys., 12, 3333-3348, doi:10.5194/acp-12-3333-2012, 2012.

766   Lelieveld, J., H. Berresheim, S. Borrmann, P.J. Crutzen, F.J. Dentener, H. Fischer, J.
767   Feichter, P.J. Flatau, J. Heland, R. Holzinger, R. Korrmann, M.G. Lawrence, Z.
768   Levin, K.M. Markowicz, N. Mihalopoulos, A. Minikin, V. Ramanathan, M. De Reus,
769   G.J. Roelofs, H.A. Scheeren, J. Sciare, H. Schlager, M. Schultz, P. Siegmund, B.
770   Steil, E.G. Stephanou, P. Stier, M. Traub, C. Warneke, J. Williams, H. Ziereis: Global
771   air pollution crossroads over the Mediterranean, Science, 298 (5594), 794-799, doi:
772   10.1126/science.1075457, 2002.

773   Levy, R. C., Remer, L. A., Mattoo, S., Vermote, E. F., and Kaufman, Y. J.: Second-
774   generation operational algorithm: Retrieval of aerosol properties over land from
775   inversion of Moderate Resolution Imaging Spectroradiometer spectral reflectance, J.
776   Geophys. Res., 112, D13211, doi:10.1029/2006JD007811, 2007.

777   Li, Z., Niu, F., Fan, J., Liu, Y., Rosenfeld, D., & Ding, Y.: Long-term impacts of aerosols
778   on the vertical development of clouds and precipitation, Nat. Geosci., 4(12), 888-894,
779   2011.

780   Ma, X., Bartlett, K., Harmon, K., and Yu, F.: Comparison of AOD between CALIPSO
781   and MODIS: significant differences over major dust and biomass burning regions,
782   Atmos. Meas. Tech., 6, 2391-2401, doi:10.5194/amt-6-2391-2013, 2013.

783   Maddy, E. S., S. G. DeSouza-Machado, N. R. Nalli, C. D. Barnet, L. L Strow, W. W.
784   Wolf, H. Xie, A. Gambacorta, T. S. King, E. Joseph, V. Morris, S. E. Hannon, and P.
785   Schou: On the effect of dust aerosols on AIRS and IASI operational level 2 products,
786   Geophys. Res. Lett., 39, L10809, doi:10.1029/2012GL052070, 2012.

787   Mallet, M., Dubovik, O., Nabat, P., Dulac, F., Kahn, R., Sciare, J., Paronis, D., and
788   Léon, J. F.: Absorption properties of Mediterranean aerosols obtained from multi-
789   year ground-based remote sensing observations, Atmos. Chem. Phys., 13, 9195-9210,
790   doi:10.5194/acp-13-9195-2013, 2013.

791   Marconi, M., Sferlazzo, D. M., Becagli, S., Bommarito, C., Calzolai, G., Chiari, M.,
792   di Sarra, A., Ghedini, C., Gómez-Amo, J. L., Lucarelli, F., Meloni, D.,
793   Monteleone, F., Nava, S., Pace, G., Piacentino, S., Rugi, F., Severi, M., Traversi, R.,
794   and Udisti, R.: Saharan dust aerosol over the central Mediterranean Sea:
795   PM_{10} chemical composition and concentration versus optical columnar

measurements, Atmos. Chem. Phys., 14, 2039-2054, doi:10.5194/acp-14-2039-2014, 2014.

Marey, H. S., Gille, J. C., El-Askary, H. M., Shalaby, E. A., and El-Raey, M. E.: Aerosol climatology over Nile Delta based on MODIS, MISR and OMI satellite data, Atmos. Chem. Phys., 11, 10637-10648, doi:10.5194/acp-11-10637-2011, 2011.

Markowicz, K. M.; Flatau, P. J.; Ramana, M. V.; Crutzen, P. J.; Ramanathan, V.: Absorbing mediterranean aerosols lead to a large reduction in the solar radiation at the surface, Geophys. Res. Lett., 29 (20), 1968, doi:10.1029/2002GL015767, 2002.

McClatchey, R. A., Fenn, R. W., Selby, J. E. A., Volz, F. E., and Garing, J. S.: Optical properties of the atmosphere. 3rd ed. AFCRL Environ. Res. Papers No. 411, 108 pp, 1972.

McComiskey, A., S. E. Schwartz, B. Schmid, H. Guan, E. R. Lewis, P. Ricchiazzi, and J. A. Ogren: Direct aerosol forcing: Calculation from observables and sensitivities to inputs, J. Geophys. Res. Atmos., 113, D09202, doi:10.1029/2007JD009170, 2008.

Mélin, F., and G. Zibordi: Aerosol variability in the Po Valley analyzed from automated optical measurements, Geophys. Res. Lett., 32, L03810, doi:10.1029/2004GL021787, 2005.

Meloni, D., di Sarra, A., DeLuisi, J., Di Iorio, T., Fiocco, G., Junkermann, W., and Pace, G.: Tropospheric aerosols in the Mediterranean: 2. Radiative effects through model simulations and measurements, J. Geophys. Res. Atmos., 108, 4317, doi:10.1029/2002JD002807, 2003.

Mielonen, T., Arola, A., Komppula, M., Kukkonen, J., Koskinen, J., de Leeuw, G., and Lehtinen, K. E. J.: Comparison of CALIOP level 2 aerosol subtypes to aerosol types derived from AERONET inversion data, Geophys. Res. Lett., 36, L18804, doi:10.1029/2009GL039609, 2009.

Moulin, C., C. E. Lambert, U. Dayan, TM V. Masson, M. Ramonet, P. Bousquet, M. Legrand, Y. J. Balkanski, W. Guelle, B. Marticorena, G. Bergametti, and F. Dulac: Satellite climatology of African dust transport in the Mediterranean atmosphere, J. Geophys. Res. Atmos., 103(D11), 13137–13144, doi:10.1029/98JD00171, 1998.

825 Nabat, P., Somot, S., Mallet, M., Chiapello, I., Morcrette, J. J., Solmon, F., Szopa, S.,
826   Dulac, F., Collins, W., Ghan, S., Horowitz, L. W., Lamarque, J. F., Lee, Y. H.,
827   Naik, V., Nagashima, T., Shindell, D., and Skeie, R.: A 4-D climatology (1979–2009)
828   of the monthly tropospheric aerosol optical depth distribution over the Mediterranean
829   region from a comparative evaluation and blending of remote sensing and model
830   products, Atmos. Meas. Tech., 6, 1287-1314, doi:10.5194/amt-6-1287-2013, 2013.

831 Omar, A.H., Winker, M.D., Vaughan, M.A., et al.: The CALIPSO automated aerosol
832   classification and lidar ratio selection algorithm. J. Atmos. Oceanic Technol. 26 (10),
833   1994-2014, 2009.

834 Oo, M. and Holz, R.: Improving the CALIOP aerosol optical depth using combined
835   MODIS-CALIOP observations and CALIOP integrated attenuated total color ratio, J.
836   Geophys. Res. Atmos., 116, D14201, doi:10.1029/2010jd014894, 2011.

837 Pace, G., di Sarra, A., Meloni, D., Piacentino, S., and Chamard, P.: Aerosol optical
838   properties at Lampedusa (Central Mediterranean). 1. Influence of transport and
839   identification of different aerosol types, Atmos. Chem. Phys., 6, 697-713,
840   doi:10.5194/acp-6-697-2006, 2006.

841 Papadimas, C. D., Hatzianastassiou, N., Matsoukas, C., Kanakidou, M.,
842   Mihalopoulos, N., and Vardavas, I.: The direct effect of aerosols on solar radiation
843   over the broader Mediterranean basin, Atmos. Chem. Phys., 12, 7165-7185,
844   doi:10.5194/acp-12-7165-2012, 2012.

845 Peña, O., and Pal, U.: Scattering of electromagnetic radiation by a multilayered sphere,
846   *Computer Physics Communications*, 180(11), 2348 - 2354, 2009.

847 Pierangelo, C., Chédin, A., Heilliette, S., Jacquinet-Husson, N., and Armante, R.: Dust
848   altitude and infrared optical depth from AIRS, Atmos. Chem. Phys., 4, 1813-1822,
849   doi:10.5194/acp-4-1813-2004, 2004.

850 Ramanathan, V., Crutzen, P. J., Lelieveld, J., Mitra, A. P., Althausen, D., Anderson, J. et
851   al.: Indian Ocean Experiment: An integrated analysis of the climate forcing and
852   effects of the great Indo-Asian haze. *Journal of Geophysical Research: Atmospheres*
853   *(1984–2012)*, *106*(D22), 28371-28398, 2001.

854   Ramanathan, V.; Chung, C.; Kim, D.; Bettge, T.; Buja, L.; Kiehl, J. T.; Washington, W.
855   M.; Fu, Q.; Sikka, D. R.; Wild, M.: Atmospheric brown clouds: Impacts on South
856   Asian climate and hydrological cycle. Proc. Natl. Acad. Sci., USA, 102 (15), 5326-
857   5333, 2005.

858   Reid, J. S., J. E. Kinney, D. L. Westphal, B. N. Holben, E. J. Welton, S. Tsay, D. P.
859   Eleuterio, J. R. Campbell, S. A. Christopher, P. R. Colarco, H. H. Jonsson, J. M.
860   Livingston, H. B. Maring, M. L. Meier, P. Pilewskie, J. M. Prospero, E. A. Reid, L.
861   A. Remer, P. B. Russell, D. L. Savoie, A. Smirnov, and D. Tanre´: Analysis of
862   measurements of Saharan dust by airborne and ground-based remote sensing methods
863   during the Puerto Rico Dust Experiment (PRIDE), J. Geophys. Res. Atmos.,
864   108(D19), 8586, doi:10.1029/2002JD002493, 2003.

865   Remer, L. A., Kleidman, R. G., Levy, R. C., Kaufman, Y. J., Tanre, D., Mattoo, S.,
866   Martins, J. V., Ichoku, C., Koren, I., Yu, H., and Holben, B. N.: Global aerosol
867   climatology from the MODIS satellite sensors, J. Geophys. Res. Atmos., 113,
868   D14S07, doi:10.1029/2007JD009661, 2008.

869   Ricchiazzi, P., Yang, S., Gautier, C., and Sowle, D.: SBDART: A research and teaching
870   software tool for plane-parallel radiative transfer in the Earth's atmosphere, Bull. Am.
871   Meteorol. Soc., 79, 2101–2114, 1998.

872   Rothman, L. S., Jacquemart, D., Barbe, A., Chris Benner, D., Birk, M., Brown, L. R.,
873   Carleer, M. R., Chackerian, C., Chance, K., Coudert, L. H., Dana, V., Devi, V. M.,
874   Flaud, J.-M., Gamache, R. R., Goldman, A., Hartmann, J.-M., Jucks, K. W., Maki, A.
875   G., Mandin, J.-Y., Massie, S. T., Orphal, J., Perrin, A., Rinsland, C. P., Smith, M. A.
876   H., Tennyson, J., Tolchenov, R. N., Toth, R. A., Vander Auwera, J., Varanasi, P., and
877   Wagner, G.: The HITRAN 2004 molecular spectroscopic database, *Journal of*
878   *Quantitative Spectroscopy and Radiative Transfer*, 96, 139, 2005.

879   Russell, P. B., R. W. Bergstrom, Y. Shinozuka, A. D. Clarke, P. F. DeCarlo, J. L.
880   Jimenez, J. M. Livingston, J. Redemann, O. Dubovik, and A. Strawa: Absorption
881   Ångstrom Exponent in AERONET and related data as an indicator of aerosol
882   composition, Atmos. Chem. Phys., 10, 1155–1169, doi:10.5194/acp-10-1155-2010,
883   2010.

884 Santese, M., Perrone, M. R., Zakey, A. S., De Tomasi, F., and Giorgi, F.: Modeling of
885   Saharan dust outbreaks over the Mediterranean by RegCM3: case studies, Atmos.
886   Chem. Phys., 10, 133–156, doi:10.5194/acp-10-133-2010, 2010.

887 Seiki, T., and Nakajima T.: Aerosol Effects of the Condensation Process on a Convective
888   Cloud Simulation. J. Atmos. Sci. doi:10.1175/JAS-D-12-0195.1, *in press,* 2013.

889 Shi, Y., Zhang, J., Reid, J. S., Hyer, E. J., Eck, T. F., Holben, B. N., and Kahn, R. A.: A
890   critical examination of spatial biases between MODIS and MISR aerosol products −
891   application for potential AERONET deployment, Atmos. Meas. Tech., 4, 2823-2836,
892   doi:10.5194/amt-4-2823-2011, 2011.

893 Sinyuk, A., B. N. Holben, A. Smirnov, T. F. Eck, I. Slutsker, J. S. Schafer, D. M. Giles,
894   and Sorokin, M.: Assessment of error in aerosol optical depth measured by
895   AERONET due to aerosol forward scattering, Geophys. Res. Lett., 39, L23806,
896   doi:10.1029/2012GL053894, 2012.

897 Stamnes, K., Tsay, C., Wiscombe, W., and Jayaweera, K.: Numerically stable algorithm
898   for discrete-ordinate-method radiative transfer in multiple scattering and emitting
899   layered media, Appl. Opt., 27, 2502–2509, 1988.

900 Stevens, B. and Feingold, G.: Untangling aerosol effects on clouds and precipitation in a
901   buffered system, Nature, 461, 607–613, 2009.

902 Tanré, D., C. Deroo, P. Duhaut, M. Herman, J. J. Morcrette, J. Perbos, and Deschamps,
903   P. Y.: Description of a computer code to simulate the satellite signal in the solar
904   spectrum: The 5S code. *Int. J. Remote Sens.,* **11** (4), 659–668, 1990.

905 Tanré, D., Y. J. Kaufman, B. N. Holben, B. Chatenet, A. Karnieli, F. Lavenu, L. Blarel,
906   O. Dubovik, L. A. Remer, and A. Smirnov: Climatology of dust aerosol size
907   distribution and optical properties derived from remotely sensed data in the solar
908   spectrum, J. Geophys. Res. Atmos., 106(D16), 18205–18217,
909   doi:10.1029/2000JD900663, 2001.

910 Vrekoussis, M., Liakakou, E., Kocak, M., Kubilay, N., Oikonomou, K., Sciare, J.,
911   Mihalopoulos, N.: Seasonal variability of optical properties of aerosols in the Eastern
912   Mediterranean, Atmos. Environ., 39 (37), 7083-7094, 2005.

913 Wang, K.-Y.: Profiles of the atmospheric temperature response to the Saharan dust
914   outbreaks derived from FORMOSAT-3/COSMIC and OMI AI, Atmos. Res., 96(1),
915   110–121, doi:10.1016/j.atmosres.2009.11.017, 2010.

916 Winker, D. M., Pelon, J., and McCormick, M. P.: The CALIPSO mission: Space borne
917   lidar for observation of aerosols and clouds, Proc. SPIE 4893, Lidar Remote Sensing
918   for Industry and Environment Monitoring III, 1, 1–11, doi:10.117/12.466539, 2003.

919 Winker, D. M., Tackett, J. L., Getzewich, B. J., Liu, Z., Vaughan, M. A., and
920   Rogers, R. R.: The global 3-D distribution of tropospheric aerosols as characterized
921   by CALIOP, Atmos. Chem. Phys., 13, 3345-3361, doi:10.5194/acp-13-3345-2013,
922   2013.

923 Wu, C. F. J.: Jackknife, bootstrap and other resampling methods in regression
924   analysis. *The Annals of Statistics*, *14*(4), 1261-1295, 1986.

925 Xiao, N., Shi, T., Calder, C. A., Munroe, D. K., Berrett, C., Wolfinbarger, S., and Li, D.:
926   Spatial characteristics of the difference between MISR and MODIS aerosol optical
927   depth retrievals over mainland Southeast Asia. *Remote Sensing of*
928   *Environment*, *113*(1), 1-9, 2009.

929 Young, S. A., and Vaughan M. A.: The Retrieval of Profiles of Particulate Extinction
930   from Cloud-Aerosol Lidar Infrared Pathfinder Satellite Observations (CALIPSO)
931   Data: Algorithm Description. J. Atmos. Oceanic Technol., **26**, 1105–1119, 2009.

932 Yu, H., Chin, M., Remer, L. A., Kleidman, R., Bellouin, N., Blan, H., and Diehl, T.:
933   Variability of marine aerosol fine mode fraction estimates of anthropogenic aerosol
934   component over cloud-free oceans from the Moderate Resolution Imaging
935   Spectroradiometer (MODIS), J. Geophys. Res. Atmos., 114, D10206,
936   doi:10.1029/2008JD010648, 2009.

937 Zhang, L., Li, Q. B., Gu, Y., Liou, K. N., and Meland, B.: Dust vertical profile impact on
938   global radiative forcing estimation using a coupled chemical-transport–radiative-
939   transfer model, Atmos. Chem. Phys., 13, 7097-7114, doi:10.5194/acp-13-7097-2013,
940   2013.

941   Zhu, A., Ramanathan, V., Li, F., & Kim, D.: Dust plumes over the Pacific, Indian, and

942   Atlantic oceans: Climatology and radiative impact. *Journal of Geophysical Research:*

943   *Atmospheres (1984–2012)*, *112*(D16), (2007).

944

945

946

947

948

949

950

951

952

953

954

955

956

957

958

959

960

961

962

963

964

965

966

967

968

969   Table 1 MODIS-derived summer-time mean AOD at 550 nm (±standard deviation)

970   within the aerosol layer over the ROI for 10 years (2003-2012).

Year	2003	2004	2005	2006	2007	2008	2009	2010	2011	2012
AOD	0.20 ±0.06	0.20 ±0.10	0.20 ±0.07	0.24 ±0.13	0.23 ±0.09	0.24 ±0.11	0.19 ±0.05	0.25 ±0.12	0.21 ±0.06	0.19 ±0.07

971

972

973

974

975

976

977

978

979

980

981

982

983

984 Table 2 Summer-time averaged optical properties of (level 2) of Mediterranean

985 AERONET sites used in this study. 'N' represents the number of level 2 observation days

986 during summer season used in analyses. The subscripts of parameters name show

987 wavelength in nm.

988

Site Name	N	$AAE_{440-870}$	$EAE_{440-870}$	AOD_{440}	SSA_{440}	$AAOD_{440}$	$ASYP_{440}$
Pollution Dominated Sites							
Athens	306	1.26±0.33	1.52±0.35	0.26±0.11	0.91±0.03	0.04±0.01	0.70±0.02
Avignon	670	1.33±0.49	1.47±0.33	0.21±0.13	0.91±0.03	0.04±0.01	0.69±0.02
Barcelona	315	1.29±0.57	1.34±0.34	0.26±0.12	0.91±0.04	0.05±0.02	0.70±0.02
Burjassot	349	1.37±0.45	1.21±0.34	0.25±0.11	0.93±0.03	0.03±0.02	0.71±0.02
Ersa	232	1.43±0.58	1.37±0.36	0.19±0.10	0.95±0.02	0.02±0.01	0.69±0.02
Ispra	462	1.33±0.28	1.62±0.22	0.41±0.32	0.93±0.03	0.04±0.02	0.71±0.03
Lecce	661	1.58±0.48	1.44±0.45	0.26±0.13	0.92±0.04	0.04±0.02	0.68±0.03
Messina	284	1.31±0.45	1.30±0.49	0.26±0.12	0.94±0.03	0.03±0.01	0.70±0.03
Modena	240	1.35±0.29	1.51±0.33	0.35±0.19	0.93±0.03	0.03±0.01	0.70±0.03
Moldova	541	1.22±0.23	1.63±0.24	0.29±0.16	0.94±0.03	0.03±0.02	0.70±0.02
Potenza	183	1.23±0.79	1.23±0.41	0.20±0.11	0.89±0.06	0.05±0.03	0.69±0.03
Rome	533	1.56±0.54	1.36±0.39	0.25±0.12	0.92±0.03	0.04±0.02	0.69±0.03
Thessaloniki	385	1.27±0.28	1.58±0.34	0.35±0.16	0.94±0.02	0.03±0.01	0.70±0.02
Toulon	365	1.34±0.43	1.53±0.33	0.20±0.11	0.94±0.02	0.03±0.01	0.69±0.02
Villefranche	353	0.93±0.39	1.55±0.34	0.25±0.15	0.95±0.02	0.03±0.01	0.70±0.02
Dust Affected Sites							
Blida	332	2.02±0.39	0.82±0.41	0.32±0.17	0.89±0.02	0.06±0.02	0.72±0.03
Malaga	302	1.55±0.45	0.88±0.34	0.23±0.13	0.89±0.03	0.05±0.02	0.72±0.03
Granada	480	1.78±0.44	0.95±0.39	0.21±0.11	0.90±0.02	0.05±0.01	0.70±0.03
Forth Crete	483	1.57±0.52	1.39±0.42	0.24±0.10	0.94±0.03	0.03±0.01	0.70±0.02
Lampedusa	276	2.24±0.61	1.01±0.56	0.26±0.14	0.91±0.03	0.04±0.02	0.71±0.03
Erdemli	536	0.95±0.31	1.36±0.24	0.37±0.16	0.94±0.03	0.03±0.02	0.71±0.02
Sde Boker	1103	1.15±0.52	1.07±0.33	0.22±0.10	0.92±0.02	0.04±0.01	0.72±0.02
Nes Ziona	432	1.02±0.41	1.23±0.32	0.30±0.14	0.93±0.04	0.04±0.02	0.72±0.03
Oristano	232	1.52±0.63	1.17±0.50	0.28±0.17	0.89±0.02	0.06±0.02	0.71±0.03

989

990

991

992 Table 3 Day-time average aerosol radiative forcing [Wm^{-2}] in short wavelength (SW) and

993 long wavelength (LW) region for different absorbing aerosols during summer 2010 over

994 the Eastern Mediterranean basin.

Aerosol Type	SW (0.25 - 4.0 μm)		LW (4 - 20.0 μm)	
	$(\Delta F_{aer})_{SRF}$	$(\Delta F_{aer})_{TOA}$	$(\Delta F_{aer})_{SRF}$	$(\Delta F_{aer})_{TOA}$
Dust	-21.95	-11.05	2.47	0.91
Polluted Dust	-39.95	-20.60	3.31	0.64
Polluted Continental	-17.41	-10.27	0.78	0.07

995

996

997

998

999

1000

1001

1002

1003

1004

1005

1006 Table 4 Summer-time observed approximated heating rate [dT/dt ±standard deviation]

1007 within the aerosol layer and MODIS-AOD (±standard deviation) over the ROI in the

1008 eastern Mediterranean Basin for 10 years (2003-2012).

Year	2003	2004	2005	2006	2007	2008	2009	2010	2011	2012
Heating [K/day]	1.4 ±0.4	1.4 ±0.7	1.4 ±0.5	1.7 ±0.9	1.6 ±0.6	1.7 ±0.8	1.3 ±0.3	1.7 ±0.8	1.5 ±0.4	1.3 ±0.4
AOD	0.2 ±0.06	0.2 ±0.10	0.2 ±0.07	0.24 ±0.13	0.23 ±0.09	0.24 ±0.11	0.19 ±0.05	0.25 ±0.12	0.21 ±0.06	0.19 ±0.07

1009

1010

1011

1012

1013

1014

1015

1016

1017

1018

1019

1020

1021

1022
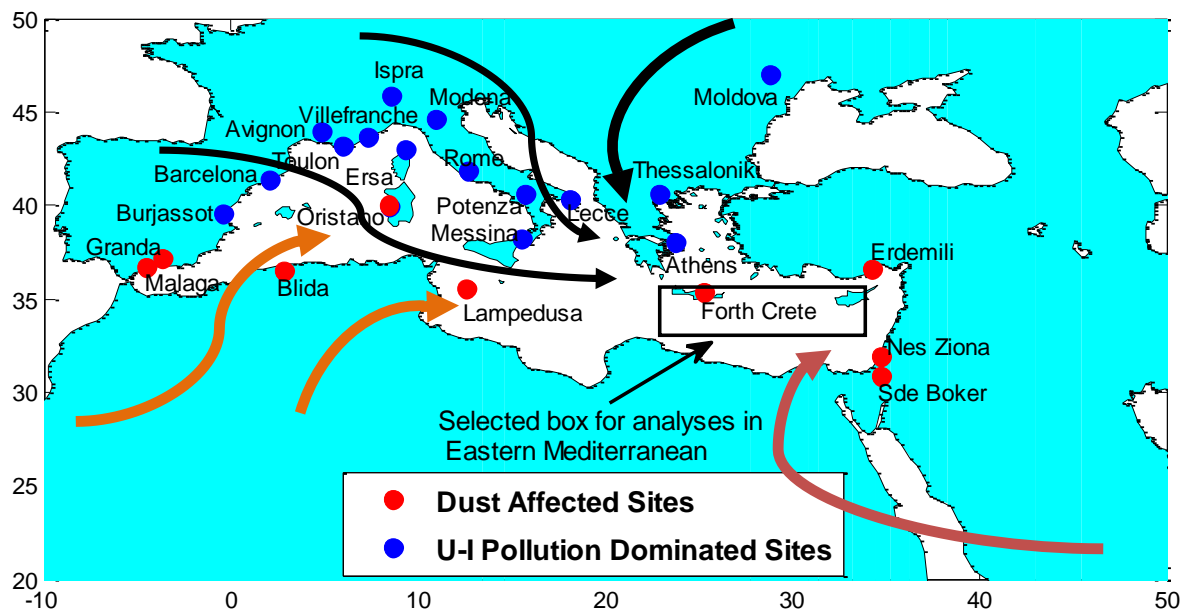
1023

1024

1025 Fig. 1 Classification of AERONET sites based on dominant aerosol types, which are
1026 likely to affect aerosol properties over the Mediterranean region. Red circles are used for
1027 dust affected sites and blue circles are used for urban-industrial (U-I) pollution dominated
1028 sites. Sites were selected based on data volume, geographic location, and primary aerosol
1029 source region. The rectangular box in the eastern Mediterranean presents our region of
1030 interest (ROI). The different color curved arrows show the schematic wind trajectories at
1031 different altitudes/time period during the summer season, 2010. The black arrows show
1032 transport of pollution from Europe, whereas light brown and dark brown show transport
1033 of dust particles from African and Arabian deserts, respectively.

1034

1035

1036

1037

1038

1039

1040
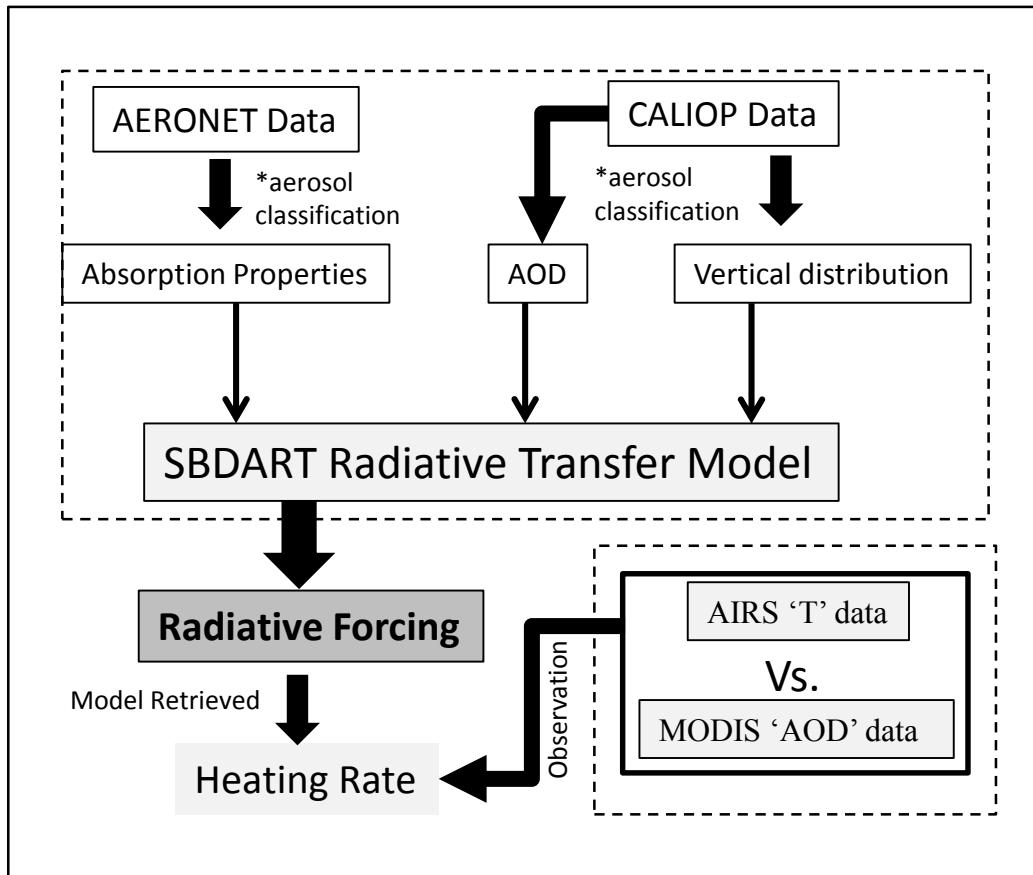
1041

1042   Fig. 2 Flow chart of the methodology. The explanations are given in text. *aerosol

1043   classification: aerosols are classified as dust, polluted dust (mixed aerosol), and polluted

1044   continental (pollution) classes. All optical and microphysical properties are derived for

1045   each class of aerosols.

1046

1047

1048
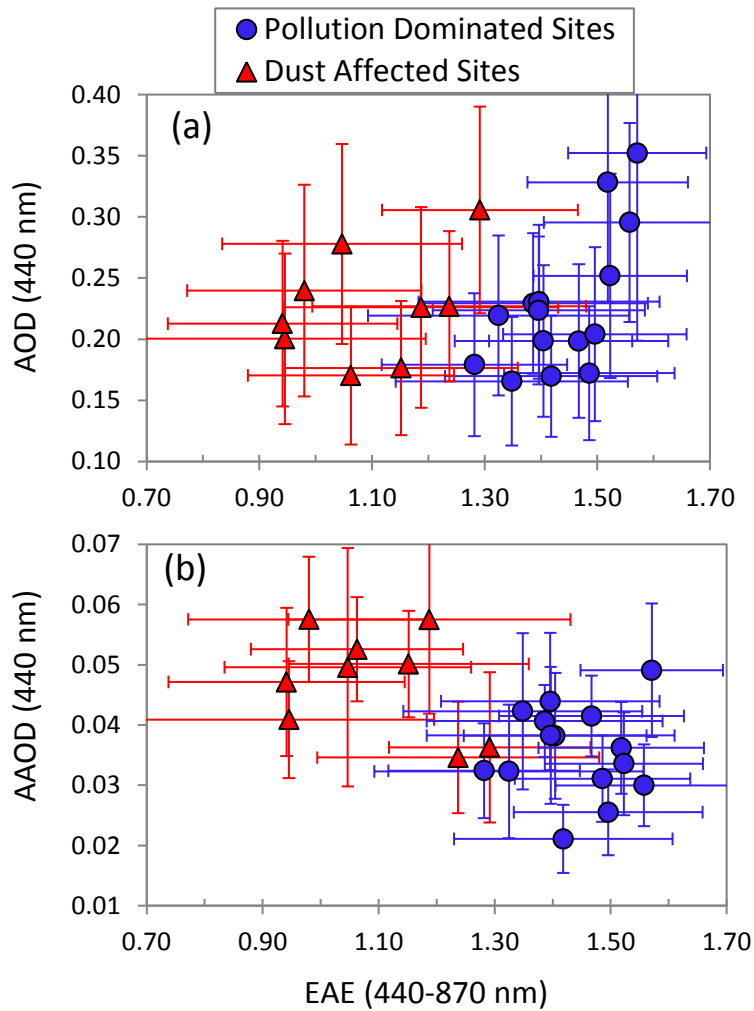
1049

Fig. 3 Average AERONET level 2 (entire data sets) scatter plots between (a) AOD vs
EAE and (b) AAOD vs EAE for the 24 selected sites in and around the Mediterranean
Basin. The red triangles represent dust affected sites and blue circles show pollution
dominated sites. The error bars represent $\pm\sigma/2$, where σ is standard deviation of
AERONET level 2 (entire) data sets for respective sites.

1050

1051

1052

1053

1054

1055

1056

1057

47
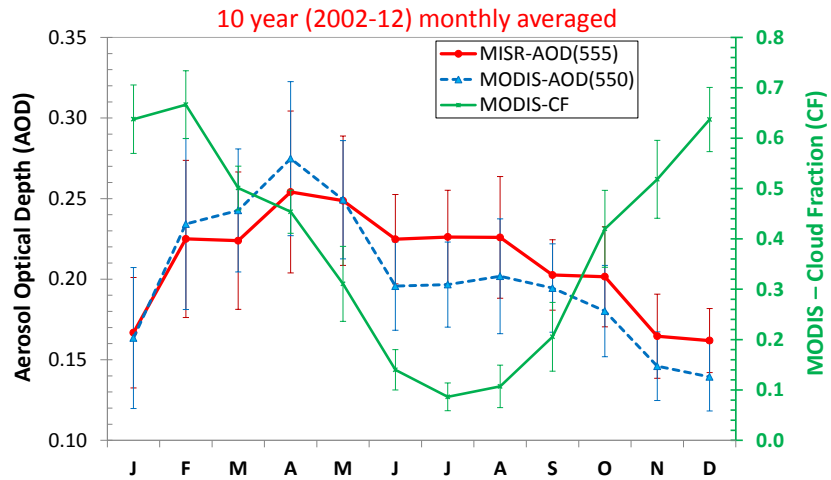
1058

1059 Fig. 4 Seasonal variation of 10 year (2002-2012) monthly averaged aerosol optical depth

1060 (AOD) and cloud fraction (CF) over the ROI observed from MODIS and MISR. Error

1061 bars represent the standard deviation of inter-annual variability.

1062

1063

1064

1065

1066

1067

1068

1069

1070

1071

1072

1073

1074

1075
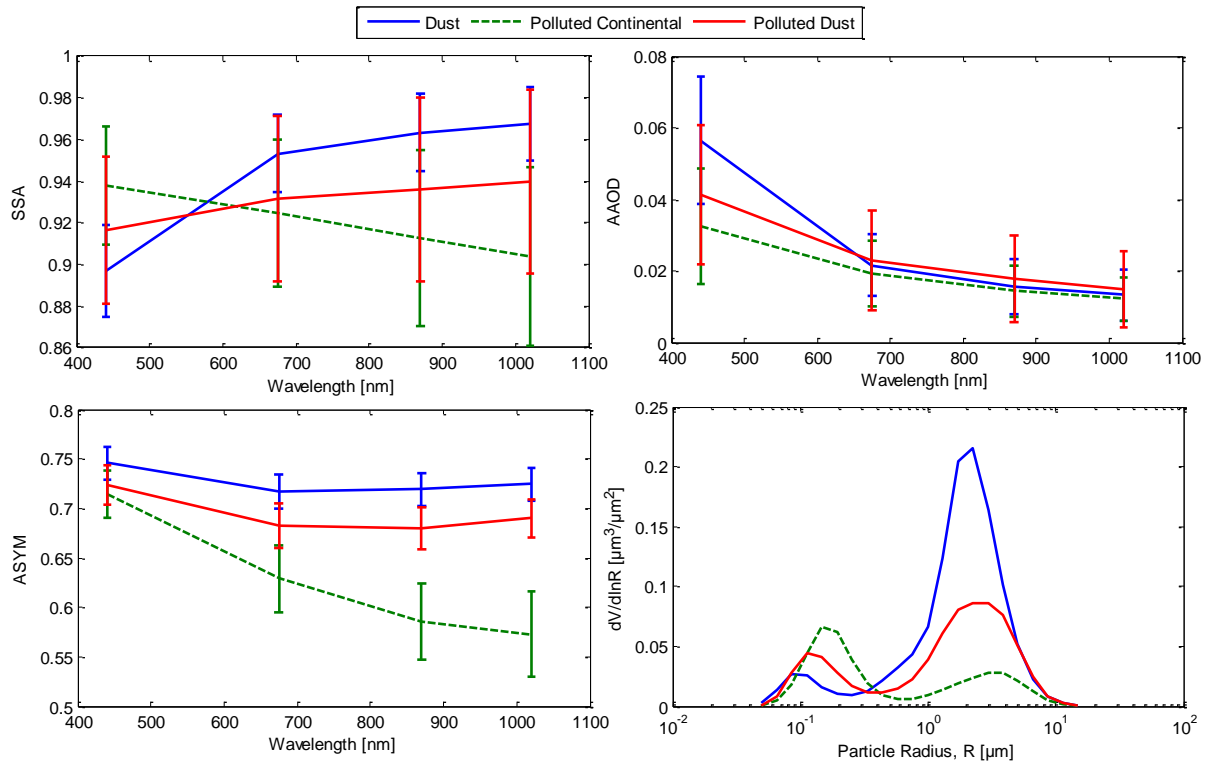
1076

Fig. 5 Spectral dependence of multi-year/multi-site average single scattering albedo (SSA), absorption aerosol optical depth (AAOD), asymmetry parameter (ASYM) and volume size distribution for dust, polluted dust and polluted continental over the Mediterranean basin. Total 259, 169 and 914 level 2 absorption data have been used to average for dust, polluted dust and polluted continental classes, respectively.

1082

1083

1084

1085

1086

1087

1088

49
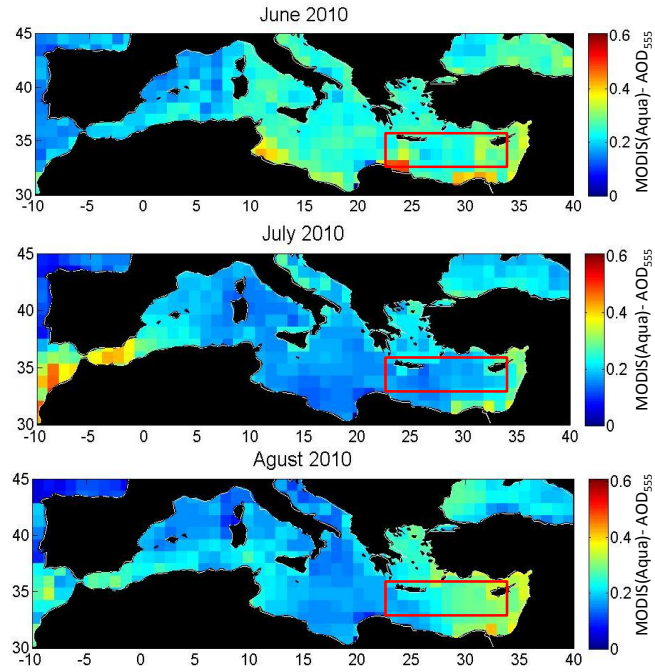
1089

1090

1091 Fig. 6 Monthly mean AOD during June – August, 2010 over the Mediterranean basin.
1092 Red rectangular boxes present the ROI.

1093

1094

1095

1096

1097

1098

1099

1100

1101

1102

1103

1104

Eastern Mediterranean Sea
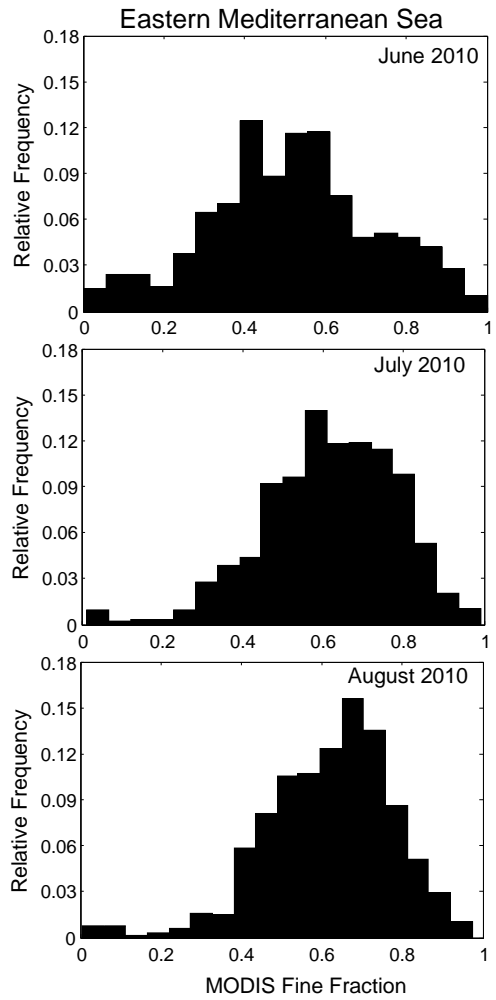
1105

1106

1107   Fig. 7 Relative frequency of MODIS Fine Fraction (ff) occurrence during June – August,

1108   2010 over the ROI.

1109

1110

1111

1112

1113

1114

1115
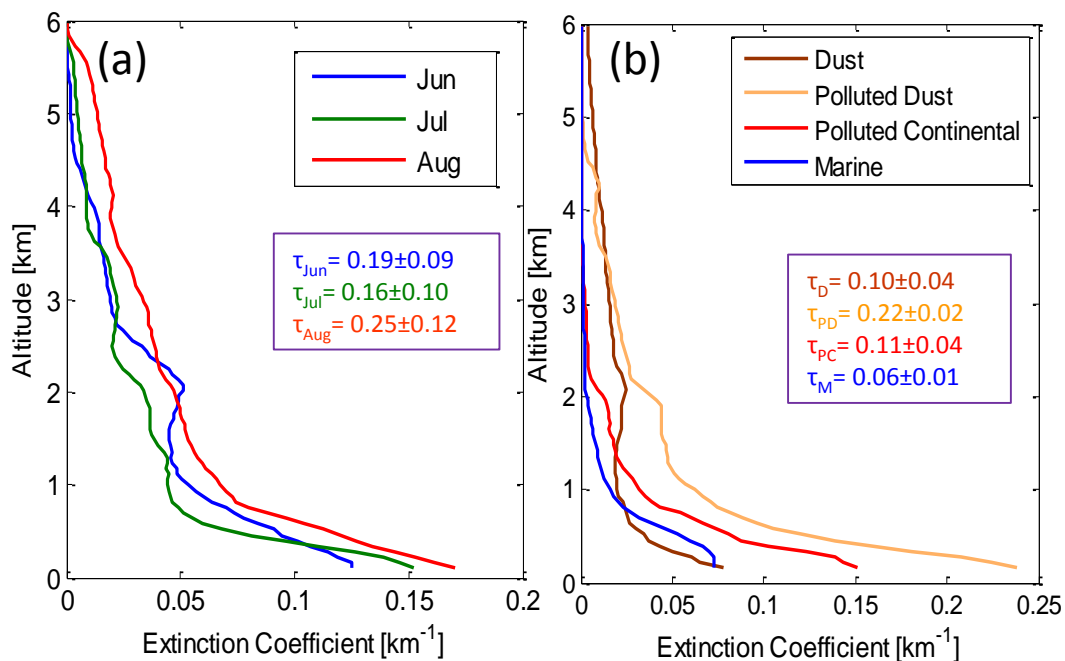
Fig. 8 Vertical distribution of mean aerosol extinction coefficient for (a) June, July and August, and (b) different dominant aerosols during summer 2010. The calculated aerosol optical depths for respective extinction profiles are given in respective colors. The standard deviations of respective means are provided in supplementary materials (Fig. S4).
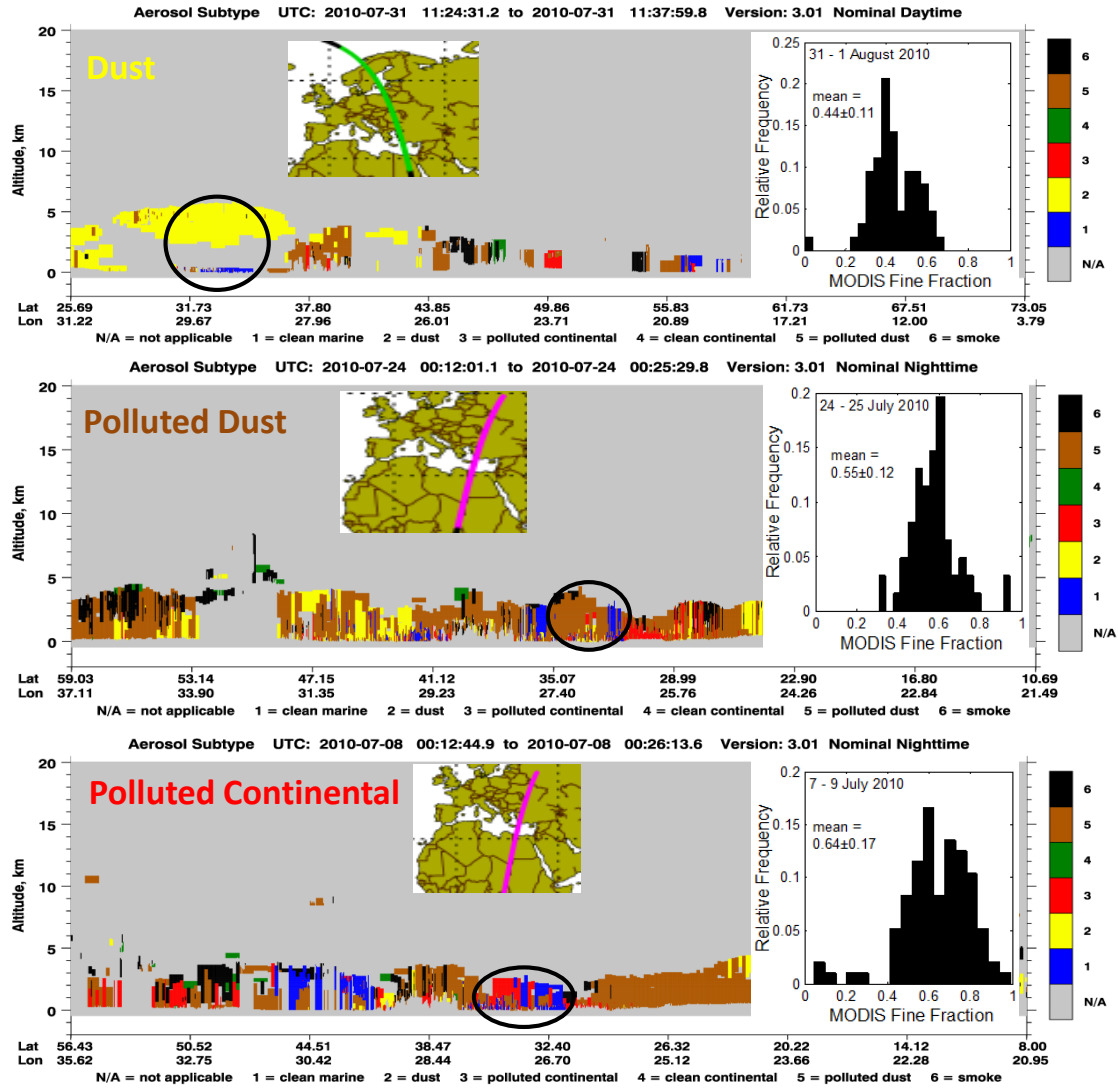
Fig. 9 Assessment of CALIOP-derived aerosol classification (vertical feature mask: VFM) using MODIS Fine Fraction (*ff*) in three different cases of dust, polluted dust and polluted continental over the ROI. The relative frequency histogram of *ff* for each case is calculated over the ROI. Approximated latitudinal extent of ROI is shown by black circles for each case in VFM figure. The various colors of VFM represent different dominant aerosol types which are marked as integer number (1-6) in respective plots. The connotations of integer numbers are given at the bottom of each plot. The marine aerosols (blue color) are present in all three cases.
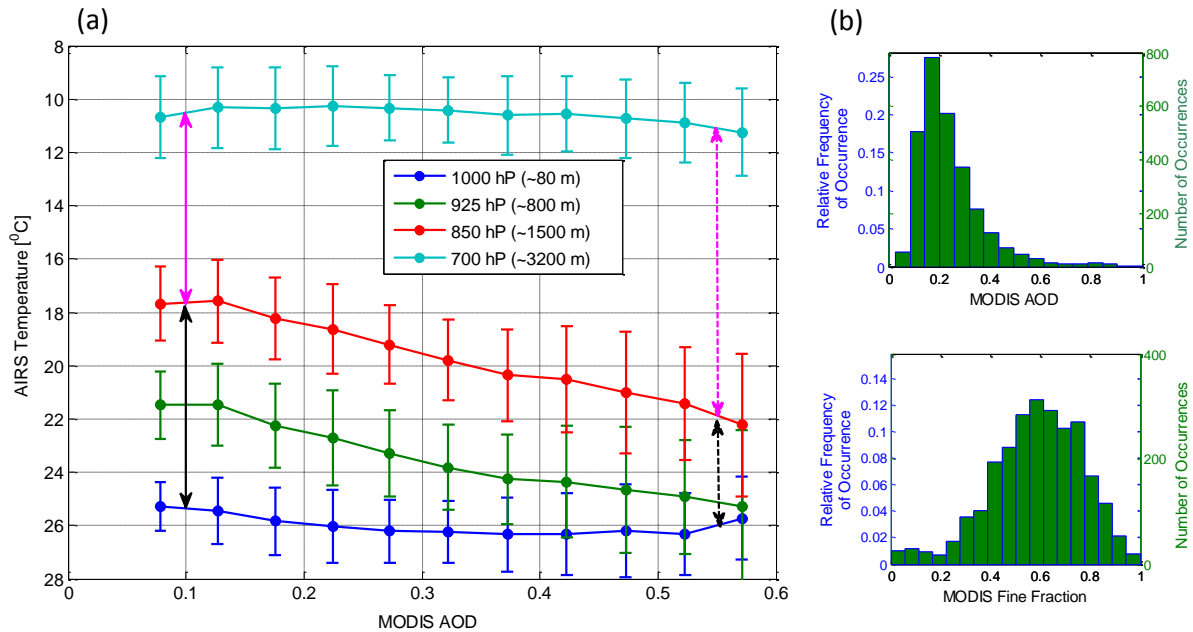
Fig. 10 (a) MODIS AOD_{550} versus AIRS temperature at 4 different pressure levels (1000, 925, 850 and 700 hP) for summer 2010. The vertical axis is in reverse order. The bold and dotted black arrows represent temperature differences between 850 and 1000 hP levels (stability parameter) in cases of clean and hazy atmosphere, respectively. Similarly, the pink arrows show temperature differences between 700 and 850 hP levels. The AIRS temperature data are sorted according to AOD and divided into equal spaced bins of 0.05 AOD_{550}. Error bars present the standard deviation of points in each bin. (b) Relative frequency distribution of occurrence (blue bar lines are relative frequency and green are number of occurrence, both are scaled) of AOD (upper panel) and *ff* (lower panel) for all observed data over the ROI.
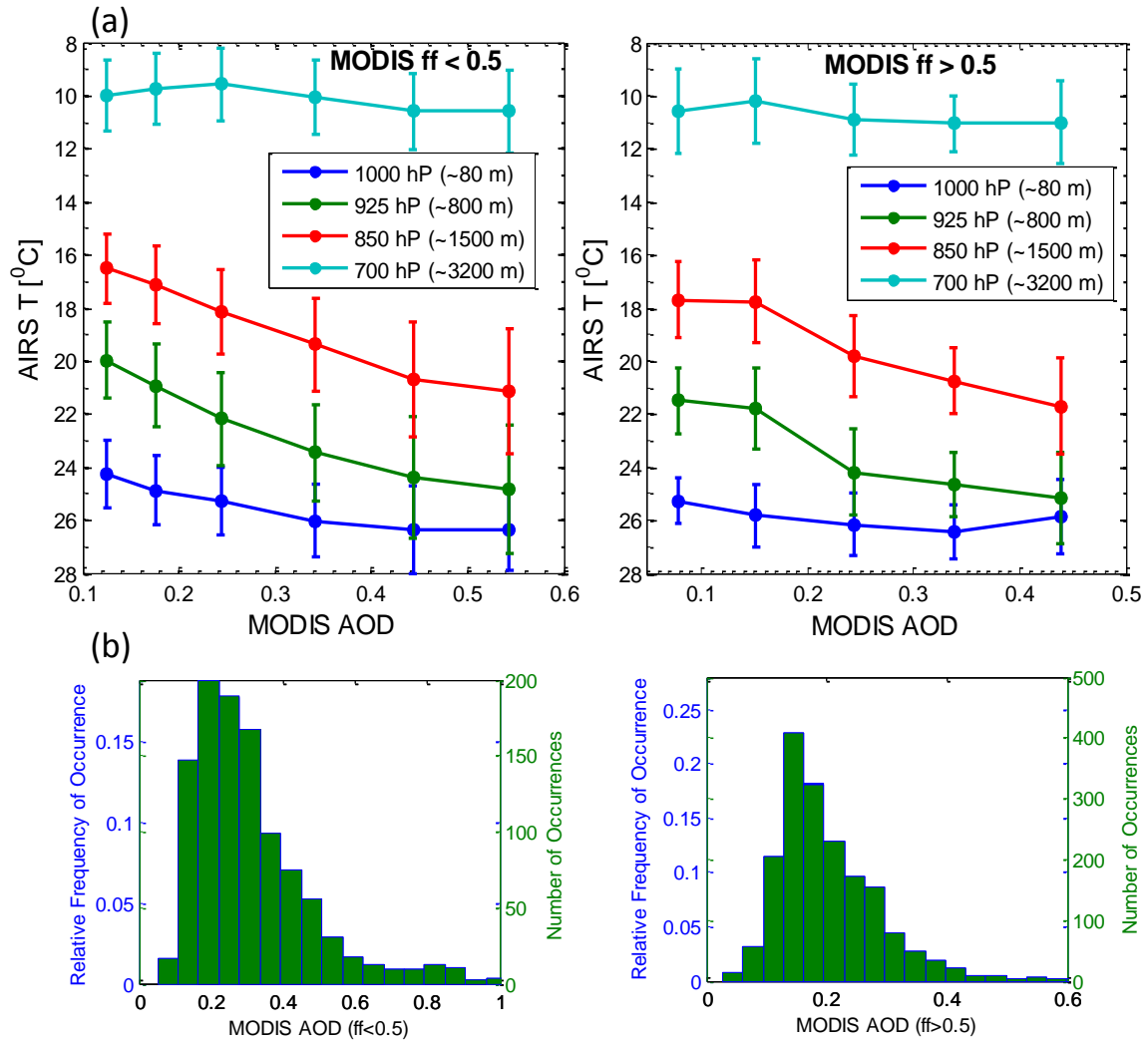
Fig. 11 Same as (a) Fig. 10a and (b) Fig. 10b (upper panel) but separated in two cases of MODIS *ff* <0.5 (left panel) and MODIS *ff*>0.5 (right panel). The horizontal axis of Fig. 11a are different for two cases (*ff*<0.5 and *ff*>0.5) as AOD binning is done according to availability of datasets.
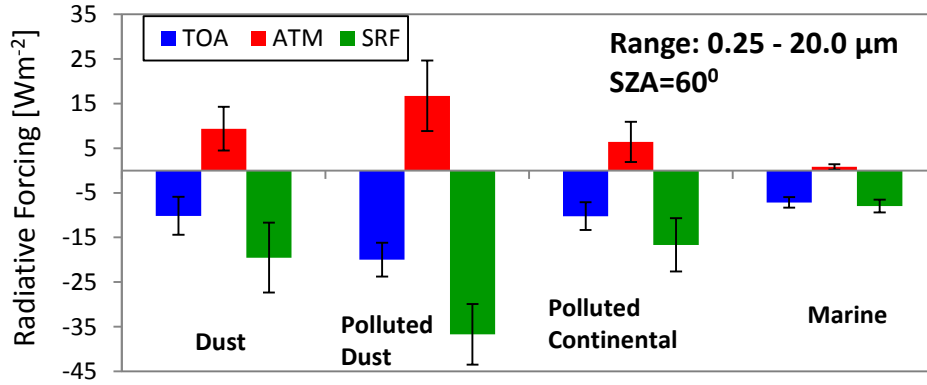
Fig. 12 Day time average radiative forcing at top of the atmosphere (TOA), at surface (SRF) and in the atmosphere (ATM) for various dominant aerosol types over eastern Mediterranean during summer 2010. The error bars present the error in calculation of radiative forcing associated with errors in major input parameters (AOD, SSA and ASYM).
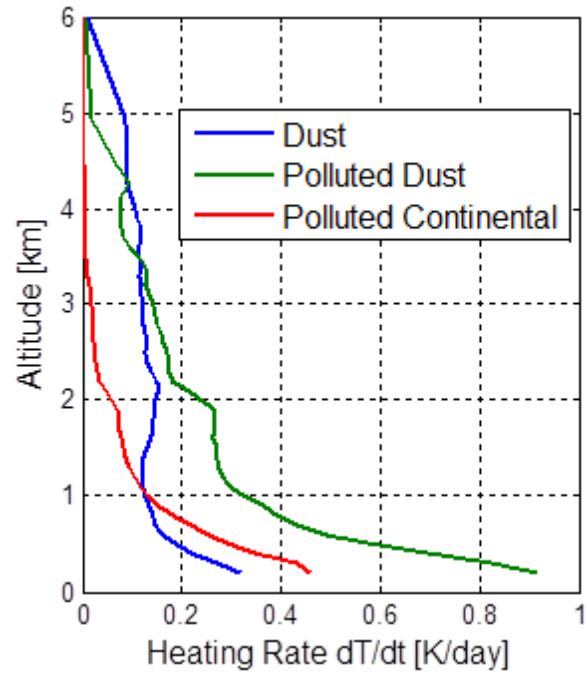
1183
1184

Fig. 13 SBDART-derived heating rate profiles of dominant absorbing aerosol types (dust, polluted dust and polluted continental) over eastern Mediterranean basin during summer 2010.

1188

1189